



HAL
open science

Microstructure study of cold rolled Al_{0.32}CoCrFeMnNi high-entropy alloy: Interactions between recrystallization and precipitation

Dorian Hachet, Stéphane Gorsse, Stephane Godet

► To cite this version:

Dorian Hachet, Stéphane Gorsse, Stephane Godet. Microstructure study of cold rolled Al_{0.32}CoCrFeMnNi high-entropy alloy: Interactions between recrystallization and precipitation. *Materials Science and Engineering: A*, 2021, 802, pp.140452. 10.1016/j.msea.2020.140452. hal-03115446

HAL Id: hal-03115446

<https://hal.science/hal-03115446>

Submitted on 29 Jan 2021

HAL is a multi-disciplinary open access archive for the deposit and dissemination of scientific research documents, whether they are published or not. The documents may come from teaching and research institutions in France or abroad, or from public or private research centers.

L'archive ouverte pluridisciplinaire **HAL**, est destinée au dépôt et à la diffusion de documents scientifiques de niveau recherche, publiés ou non, émanant des établissements d'enseignement et de recherche français ou étrangers, des laboratoires publics ou privés.

Microstructure study of cold rolled Al_{0.32}CoCrFeMnNi high-entropy alloy: interactions
between recrystallization and precipitation

Dorian Hachet^{1,*}, Stéphane Gorsse², Stéphane Godet¹

*Corresponding author

¹4MAT, Université libre de Bruxelles, 50 av. F.D. Roosevelt (CP165/63), 1050 Brussels, Belgium

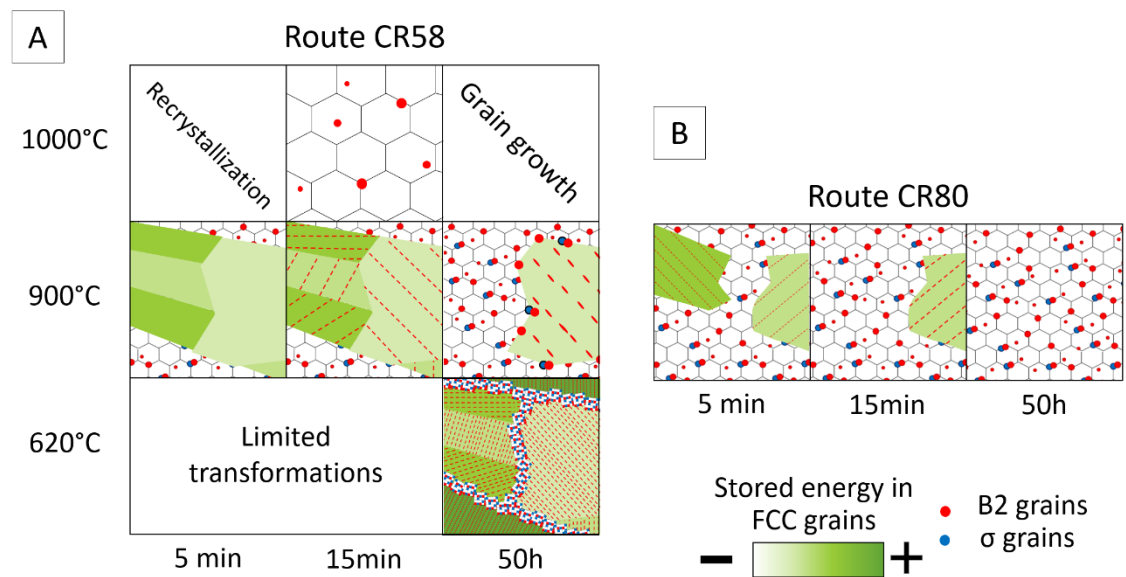
²CNRS, Univ. Bordeaux, Bordeaux INP, ICMCB, UMR 5026, F-33600, Pessac, France

Dorian Hachet : **M** dorian.hachet@ulb.ac.be, **T** +32 (0)26506550 – **F** +32 (0)26502786

Stéphane Gorsse : **M** stephane.gorsse@icmcb.cnrs.fr, **T** +33 (0)540006321

Stéphane Godet : **M** stephane.godet@ulb.ac.be, **T** +32 (0)26503648 – **F** +32 (0)26502786

Graphical abstract



Keywords: high-entropy alloy; thermomechanical treatment; recrystallization; precipitation; CALPHAD

1. Introduction

Conventional alloy design involves the development and optimization of alloys consisting of a major element together with alloying additions. In recent years, a new type of alloys called high-entropy alloys (HEAs) or complex concentrated alloys (CCAs) was developed by rethinking this paradigm [1–3]. HEAs are the combination of several elements mixed in almost equimolar proportions to form concentrated blends. While Gibbs' phase rule would predict a large number of stable phases due to the presence of a large number of constituents, it has been shown that alloys of this new family very often leads to simple microstructures and can even be single-phase [1,2]. This particular feature has been explained by considering their high configurational entropy resulting in the stabilization of single-phase disordered solid solutions over intermetallics [4]. However, this explanation is not shared by the whole community and is largely debated [5–7].

Cantor's alloy, of composition CoCrFeMnNi, is one of the most widely studied high-entropy alloys so far, which is at least partly due to its remarkable properties when tensile tested down to cryogenic temperatures. Indeed, from 20°C to -196°C, both its strength and ductility increase [8]. While the strengthening of the material is a typical consequence of the decrease in temperature, the increase in ductility is rarely encountered. In the best cases, cryogenic steels have constant ductility from ambient to cryogenic temperatures [9–13]. These remarkable properties at cryogenic temperatures are attributed to its single-phase face centred cubic (FCC) microstructure [1] and to the intensification of mechanical twinning when the temperature decreases [14].

It has been shown on conventional alloys that the presence of a second phase could lead to significant mechanical property improvements when the microstructure is optimized [15–18]. Following this strategy, several studies report the effects of modifying the chemical composition of Cantor's alloy. The strategies implemented so far are numerous: non-equiatom compositions [19–22]; small additions of interstitial elements like carbon or boron leading to solid solution strengthening and to the precipitation of inclusions [23–27]; or small additions of new elements in substitution like copper or titanium resulting in the stabilization of new phases [28–31]. Nevertheless, the strategy the most implemented is the addition of aluminium which leads to the stabilization of the ordered B2 phase [32–46,46–60]. The presence of the B2 phase induces a strengthening of the material that can be at the expense of ductility when its formation is not well controlled. While many studies have focused on as-cast materials [1,23,25,28,30,32,43,46,49–51,55,61–70,70–73], several recent studies used thermomechanical treatments with the objective of better controlling their final microstructures [31,74–88]. For example, the recent work of R. Banerjee *et al.* [81–87] on the Al_{0.3}CoCrFeNi composition, containing 7 at.% of aluminium, resulted in a wide range of tensile properties with yield strengths ranging from 160 MPa to 1800 MPa depending on the thermal history after cold rolling [83]. Similarly, the Al_{0.5}CoCrFeMnNi composition, containing 9 at.% of

aluminium, presents mechanical properties that are directly linked to its thermomechanical history [89]. Moreover, when tensile tested at cryogenic temperatures, its ductility is constant for microstructures containing up to 11 vol.% of B2 precipitates [90].

All studies cited above are interested in the *final* microstructures obtained after completion of the thermomechanical treatments. They often use large deformation levels, e.g. cold rolling reductions of 90% [81,82], in order to reach in the shortest annealing times the desired microstructures and to ensure their homogeneity. Then, the microstructure and mechanical properties are analysed. Complementing these papers, the present study focuses on the microstructure formation sequence resulting in these final microstructures. The different microstructure transformation mechanisms activated *during* the annealing treatment, and their interactions, will be detailed. More specifically, this study focuses on the $\text{Al}_{0.32}\text{CoCrFeMnNi}$ composition, including 6 at.% of aluminium, referred as C6Al (for Cantor + 6 at.% of aluminium) hereafter. This composition was kept as close as possible to Cantor's to benefit from the wide literature on this alloy as a base reference. 6 at.% of aluminium were added to ensure the precipitation of B2 during thermomechanical treatment [34]. Two thermomechanical routes characterized by two cold rolling levels are studied. The first route results in slow rates in the microstructure evolution. It is used to identify clearly the different mechanisms involved, including recrystallization and precipitation, and to understand their interactions. The influence of the annealing temperature and time are analysed based on this thermomechanical route. Then, a second route resulting in faster rates enables to analyse the influence of cold rolling strain. The respective roles of the involved mechanisms and the importance of their interactions will be discussed on the basis of thermodynamic calculations.

2. Materials and methods

2.1. Material composition

ThermoCalc software with inputs from the TCHEA4 thermodynamic database was used to predict the phase equilibria in Cantor's alloy as a function of aluminium addition (**Fig. 1**). The calculated isopleth shows that the addition of 6 at.% of aluminium results in the formation of the B2 phase below 1100°C in agreement with the observations from the literature. The σ phase is also predicted to form below 920°C. In addition, the composition allows a full FCC field to be maintained between 1150 and 1290°C. This is consistent with the need to carry out hot working of these potential industrial alloys in the FCC phase.

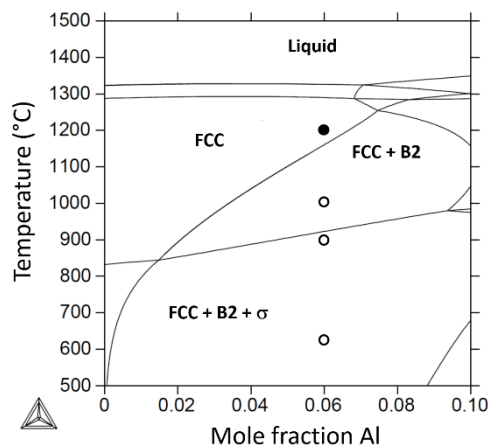


Fig. 1 CoCrFeMnNi + Al phase diagram. The studied composition $Al_{0.32}CoCrFeMnNi$ corresponds to an addition of 6 at.% of aluminium. The solid circle indicates the hot rolling temperature. The open circles indicate the three annealing temperatures considered in this study : 620, 900 and 1000°C.

Two 1kg ingots were cast in a vacuum induction furnace. Their compositions were analysed by inductively coupled plasma linked to optical emission spectroscopy (ICP-OES). The results are reported in **Table 1** together with the targeted composition. The two ingots present identical compositions. As will become clear, each ingot will be submitted to different cold rolling reduction, i.e. 58% and 80% (denoted CR58 and CR80) for ingots 1 and 2, respectively.

Table 1 Chemical compositions of the investigated ingots measured with ICP-OES along with the targeted composition, in atomic percent.

	Al	Co	Cr	Fe	Mn	Ni
--	----	----	----	----	----	----

Theoretical (at.%)	6	18.8	18.8	18.8	18.8	18.8
ICP (at.%) – CR58	6.1 ± 0.1	18.8 ± 0.1	18.1 ± 0.5	19.2 ± 0.4	19.1 ± 0.2	18.8 ± 0.1
ICP (at.%) – CR80	5.8 ± 0.1	19.1 ± 0.2	17.9 ± 0.1	18.8 ± 0.1	19.1 ± 0.2	19.3 ± 0.1

2.2. Material processing

The material was submitted to the processing routes presented in **Fig. 2** consisting first of a hot rolling step at 1200°C for a total reduction of 70% ($\epsilon_{VM}=1.4$) followed by water quenching. The first route consisted of a homogenization step at 1200°C for 24 hours and of cold rolling (CR) for a total reduction of 58%, which corresponds to a true Von Mises strain of $\epsilon_{VM}=1.0$. This route is called route CR58 according to the applied cold rolling reduction. The material was then annealed at various temperatures ranging from 620 to 1000°C for 50 hours. At the annealing temperature of 900°C, additional annealing times from 5 minutes to 750 hours have also been investigated. The second route called route CR80 consists of a cold rolling step to a reduction of 80% ($\epsilon_{VM}=2.0$) directly after hot rolling. It was then annealed at 900°C for times ranging from 5 minutes to 750 hours. All the annealing steps, following both CR58 and CR80, were performed under argon atmosphere and followed by air cooling.

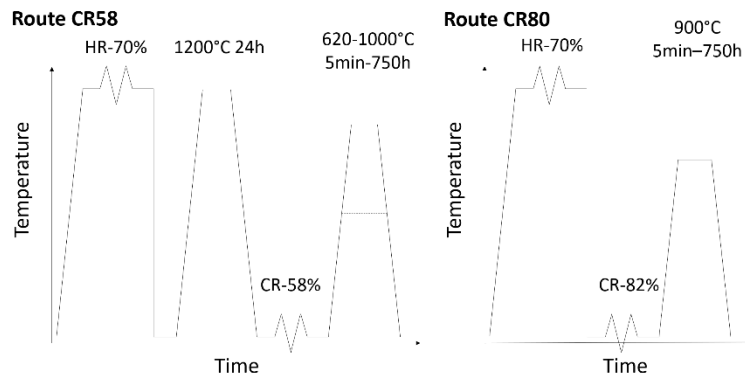


Fig. 2 Schematics of the two thermomechanical schedules chosen for processing of C6Al.

2.3. Microstructure characterization

Microstructure characterization was performed on the sections containing the RD and ND directions. The samples were conventionally prepared. They were first polished down to 3 μm using diamond paste. The last polishing step was then performed during 30 minutes using OPU solution containing a 40 nm colloidal silica suspension.

The recrystallized fraction was determined using optical microscopy, by systematic manual point counting [91] using ImageJ software. A minimum of ten images were acquired for each set of processing parameters. SEM characterization was conducted using a Hitachi SU70 FEG-SEM coupled with energy dispersive spectroscopy (EDS) and electron backscattered diffraction (EBSD), operated at a voltage of 20 kV. The EBSD data were recorded with a step of 0.15 μm and analysed with TSL[®] OIM Analysis[™] software. They were always cleaned before being used for quantification. First, a grain dilation step was conducted with a grain tolerance angle of 5° and a minimum grain size of 5 pixels. The same parameters were used for the confidence index standardization. Finally, the grains presenting a confidence index lower than 0.1 were removed. Phase identification and quantification were conducted by X-ray diffraction (XRD) using a Cu K α source. The crystallographic texture was measured by XRD using a Mo K α source. The (111), (200), (220) and (331) pole figures were measured and treated with DIFFRAC.TEXTURE software. The samples were also characterized using TEM. For this purpose, the samples were mechanically thinned to approximately 100 μm and electrochemically thinned by a twinjet electropolisher. The electrolytical thinning process was performed by immersing the samples in a mixture of 10 vol.% perchloric acid in ethanol at 30 V and -15°C. Hardness was measured with a Vickers indenter using a load of 500g. The results of ten randomly spread indentations were averaged. All those observations are coupled with thermodynamic simulations performed by using the CALPHAD method with inputs from the TCHEA4 thermodynamic database from ThermoCalc software.

2.4. Mechanical characterization

Dog-bone-shaped tensile specimens with gauge length of 3 mm and width of 6 mm were machined from the rolled and annealed sheets after route CR80. Both sides of specimens were ground using SiC paper to achieve final thickness of 1.28 – 1.4 mm. Tensile tests were performed at an engineering strain rate of $2 \cdot 10^{-3} \text{ s}^{-1}$.

2.5. Nomenclature

In what follows, the different samples are referred to using their thermomechanical schedule. For example, the sample submitted to a cold rolling reduction of 58% with an additional annealing treatment at 900°C for 50 hours is referred to as CR58-900°C/50h.

We will now turn to the results. The results corresponding to the heat-treatments carried out on the samples cold rolled to a reduction of 58% will be presented first. The results on the larger reduction of 80% will then be presented.

3. Results

3.1. Microstructures before and after cold rolling

The microstructure before cold rolling in route CR58 is homogeneous and consists of equiaxed grains containing annealing twins. The grain size is $410 \pm 150 \mu\text{m}$. The material is fully FCC.

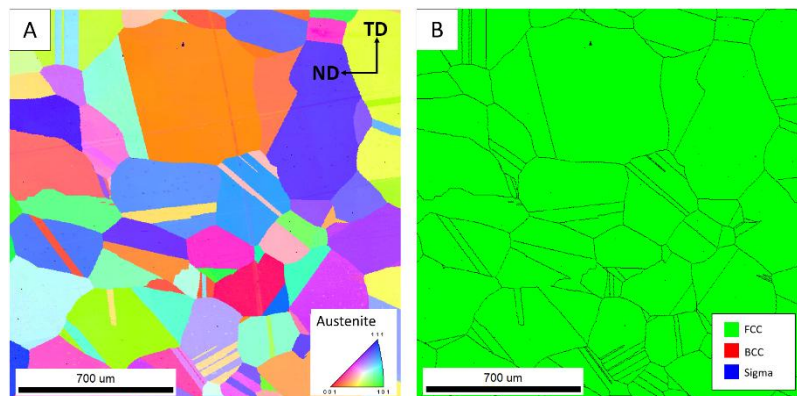


Fig. 3 Before cold rolling in route CR58. (A) IPF map, (B) phase map.

After cold rolling to a reduction of 58%, the material presents elongated grains as long as 1 millimetre in length. Intragranular misorientations are observable with strong colour gradients on the IPF map (**Fig. 4a**). The hardness is $341 \pm 12 \text{HV}0.5$. Deformation twins are observed in most grains. They are characterized by 60° misorientation boundaries as shown on the misorientation profile measured along the black line in **Fig. 4a**. The microstructure of the

alloy is a single-phase solid solution with FCC structure (**Fig. 4b**). **Fig. 4c** presents the $\Phi_2=45^\circ$ section of the orientation density function (ODF) measured by XRD. The crystallographic texture consists of the α fibre with the $\langle 110 \rangle$ direction parallel to ND. This texture is spread from Goss ($\Phi_1=90^\circ$) to A ($\Phi_1=40^\circ$) texture components (TCs). It exhibits a maximum for the Goss component with a value of 5.7 times random.

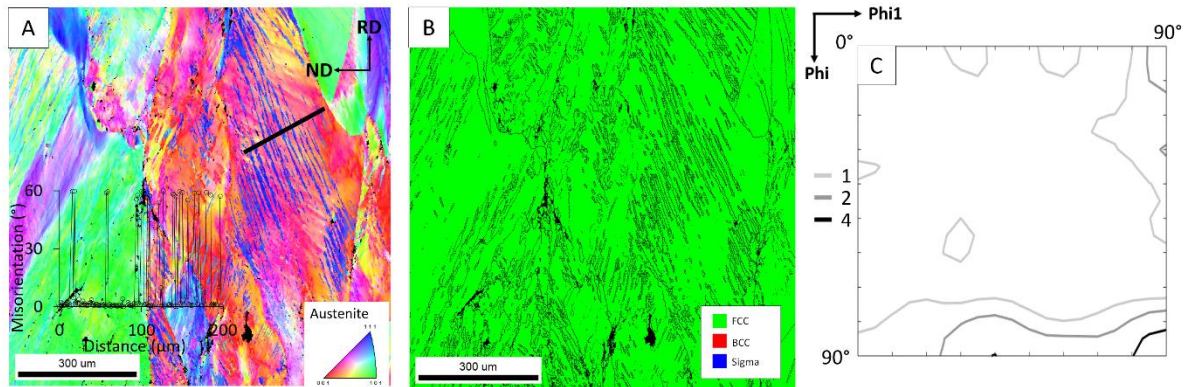


Fig. 4 CR58. (A) IPF map, (B) phase map, (C) deformation texture, $\Phi_2=45^\circ$ ODF section.

3.2. Annealing treatments after CR58

The following results will focus first on the microstructures obtained after annealing treatments at 900°C for 50 hours and then for shorter times. The microstructures obtained after annealing treatments at 620°C for 50 hours and 1000°C for 15 minutes will be detailed next.

The sample CR58- $900^\circ\text{C}/50\text{h}$ consists of two zones with distinct microstructures (**Fig. 5**). First, the region located in the middle of the EBSD maps is composed of equiaxed and strain free FCC, BCC and σ grains. As will become clear later, the BCC phase is the B2 phase, consistent with the calculated phase diagram. The mean grain sizes are 8 ± 0.3 and $1.5 \pm 0.3 \mu\text{m}$ for the FCC and the second phases, respectively. The second phases are mainly present on the grain boundaries. Interestingly, the σ grains are always located next to at least one B2 grain. Secondly, on the sides of the maps, larger FCC grains are present with occasional deformation twins inherited from cold rolling. Precipitation of elongated B2 grains is observable within this zone. These B2 grains show a mean length of $1 \pm 0.5 \mu\text{m}$ for a width of $0.3 \pm 0.1 \mu\text{m}$. The

zoomed view in **Fig. 5b** highlights the alignment of the B2 needles with the $\{111\}$ plane traces depicted by the 4 black lines. In addition, the FCC/B2 interfaces respecting the Kurdjumov-Sachs (K-S) orientation relationship (OR) are highlighted in yellow in **Fig. 5b**. It is interesting to note that the intragranular B2 grains present K-S OR on all their boundaries. It is visible in the zoomed view in **Fig. 5b**. Unlike intragranular B2 grains, the B2 grains formed on recrystallized FCC grain boundaries present a K-S OR with only one of its FCC neighbours. The centre region containing equiaxed grains will be called recrystallized zones (RXZs) as opposed to the non-recrystallized zones (nRXZs) consisting of the larger FCC and elongated B2 grains. The RXZs and nRXZs present hardness values of 250 ± 6 HV0.5 and 281 ± 5 HV0.5, respectively.

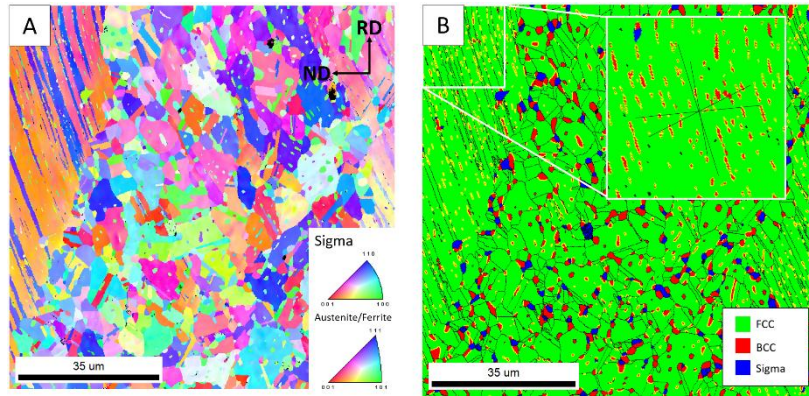


Fig. 5 CR58-900°C/50h. (A) IPF map, (B) phase map. The black lines on the phase map correspond to grain boundaries with misorientation angles larger than 15° . The yellow lines correspond to the grain boundaries between two grains obeying the K-S OR.

Two regions have been analysed by TEM in order to precise the nature of, first, the B2 and FCC phases (**Fig. 6a**) and of the σ phase (**Fig. 6b**). **Fig. 6c-e** presents the corresponding diffraction patterns. The B2 phase is ordered as shown by the sublattice spots encircled in **Fig. 6c**. This is the B2 phase in agreement with CALPHAD predictions. The matrix corresponds to a FCC lattice structure (**Fig. 6d**). The diffraction pattern of **Fig. 6e** corresponds to primitive tetragonal which is typical of the lattice structure of the σ phase. The chemical compositions of these three phases were measured by averaging 10 EDS data points (**Table 2**).

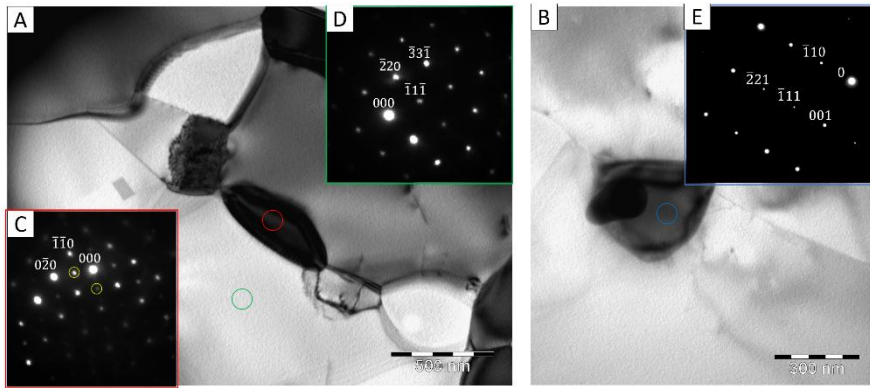


Fig. 6 TEM observations of a recrystallized zone. (A-B) bright field images, (C-E) diffraction patterns recorded in (C) a B2 grain (red circle) with sublattice spots encircled in yellow ([001] zone axis), (D) a FCC grain (green circle) ([011] zone axis), (E) a sigma grain (blue circle) ([110] zone axis).

Table 2 Chemical compositions measured with EDS of the different phases present after 50 hours at 900°C in atomic percent.

	Al (at.%)	Co (at.%)	Cr (at.%)	Fe (at.%)	Mn (at.%)	Ni (at.%)
FCC	5 ± 1	19 ± 1	20 ± 1	20 ± 1	20 ± 1	17 ± 1
B2	22 ± 2	13 ± 1	7 ± 3	8 ± 2	20 ± 1	31 ± 3
σ	2 ± 2	17 ± 1	41 ± 3	19 ± 1	16 ± 1	6 ± 2

BSE SEM micrographs of CR58-900°C/5min and CR58-900°C/15min samples are presented in **Fig. 7**. The microstructure of CR58-900°C/5min is divided between RXZs and deformed grains (**Fig. 7a**). The RXZs are located mostly on the right-hand side and composed of equiaxed FCC grains in grey with a mean grain size of $1 \pm 0.3 \mu\text{m}$. The B2 grains in black and σ grains in white present a similar mean grain size of $0.5 \pm 0.3 \mu\text{m}$. The deformed grains are composed of deformed FCC grains in shades of grey. When the annealing time is increased to 15 minutes, black needles of B2 lattice structure appear in the deformed grains located on the left-hand side of **Fig. 7b**. These needles present a length of $130 \pm 70 \text{ nm}$ and a width of $60 \pm 20 \text{ nm}$ at this stage of the annealing treatment.

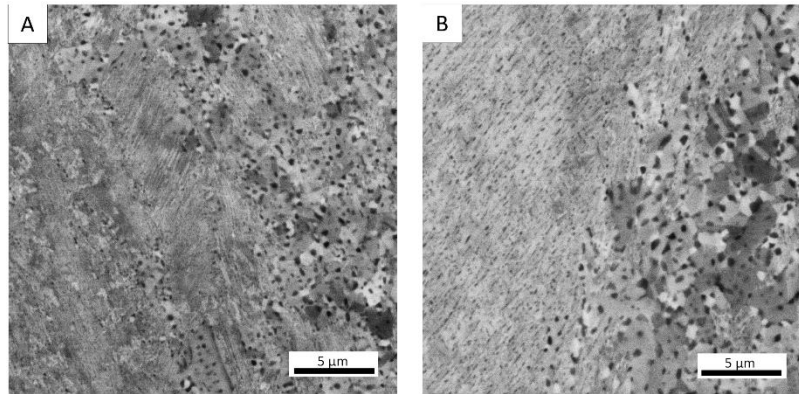


Fig. 7 Backscattered electron (BSE) micrographs acquired after annealing treatments at 900°C for (A) 5 minutes and (B) 15 minutes.

The microstructure of CR58-620°C/50h is also composed of both RXZs and nRXZs (**Fig. 8a-b**). nRXZs consist of elongated FCC grains longer than the scan. RXZs consist of equiaxed grains organized in bands spread heterogeneously in the sample (**Fig. 8a**). The zoomed view in **Fig. 8b** depicts two of these bands. These grains are FCC, B2 or the σ phase. The mean grain size of the FCC grains is $1.2 \pm 0.3 \mu\text{m}$ while it is $0.5 \pm 0.3 \mu\text{m}$ for the two second phases. The mean hardness was measured to be $486 \pm 14 \text{ HV0.5}$ – compared to the hardness of $341 \pm 12 \text{ HV0.5}$ after cold rolling –, accounting mainly for the nRXZs because of the small size and proportion of the RXZs.

The microstructure of CR58-1000°C/15min is composed of strain free FCC grains with a mean grain diameter of $8.0 \pm 9.0 \mu\text{m}$ (**Fig. 8c-d**). A small proportion (1%) of B2 precipitates is spread randomly in the material. Those B2 grains are much smaller than the FCC grains with an average diameter of $0.50 \pm 0.08 \mu\text{m}$. The σ phase does not form at this annealing temperature. The hardness level is $168 \pm 10 \text{ HV0.5}$.

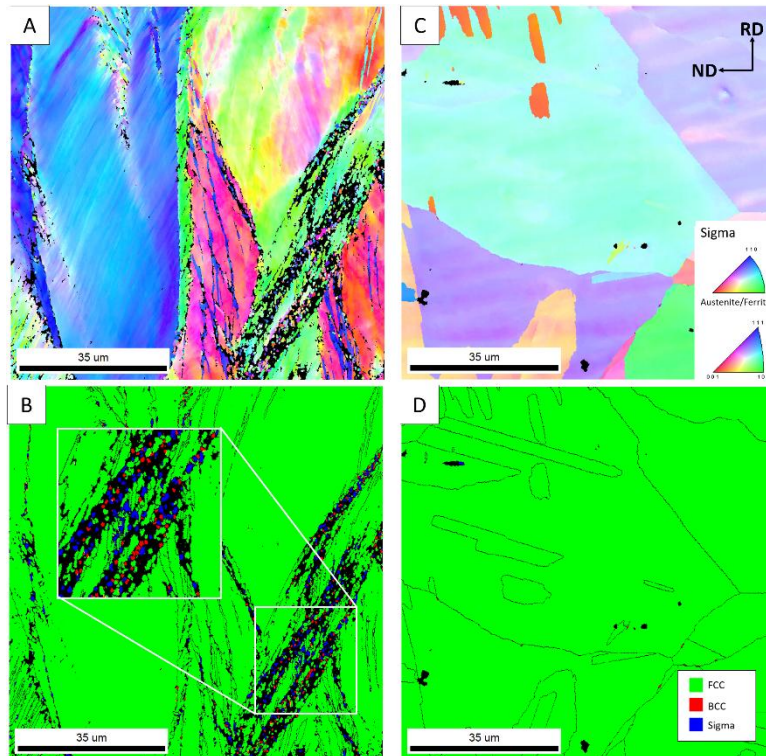


Fig. 8 EBSD maps. (A, C) are IPF maps and (B, D) phase maps measured on CR58-620°C/50h (A-B) and CR58-1000°C/15min (C-D). The black lines on phase maps correspond to grain boundaries with misorientation angles larger than 15°.

Fig. 9a presents the evolution of the volume fraction of recrystallized FCC grains with the annealing temperature, for a constant annealing time of 50 hours. Annealing temperatures of 620, 700, 800, 900 and 1000°C were studied. The recrystallized fraction is 14% after 50 hours at 620°C and then increases with the annealing temperature until reaching complete recrystallization after 50 hours at 1000°C. **Fig. 9b** shows four XRD diffractograms measured after cold rolling and further annealing treatments at 620, 900 and 1000°C for 50 hours. The FCC phase is present in all samples. A BCC phase appears during annealing treatments at 620°C and 900°C. This phase is identified as the B2 phase as was observed by TEM. The peaks corresponding to the σ phase are also present under these two annealing conditions. **Fig. 9c** presents the volume fractions of the B2 and σ phases quantified with Topas software after annealing treatments of 50 hours at 620, 700, 800, 900 and 1000°C. The second phase fractions calculated using ThermoCalc are also shown. The fractions of the B2 and σ phases reach the maxima of 28% and 5% after annealing treatments at 700°C and 800°C, respectively.

It is interesting to note that the evolution of B2 fraction agrees well with thermodynamic calculations whereas it is not the case for the σ phase.

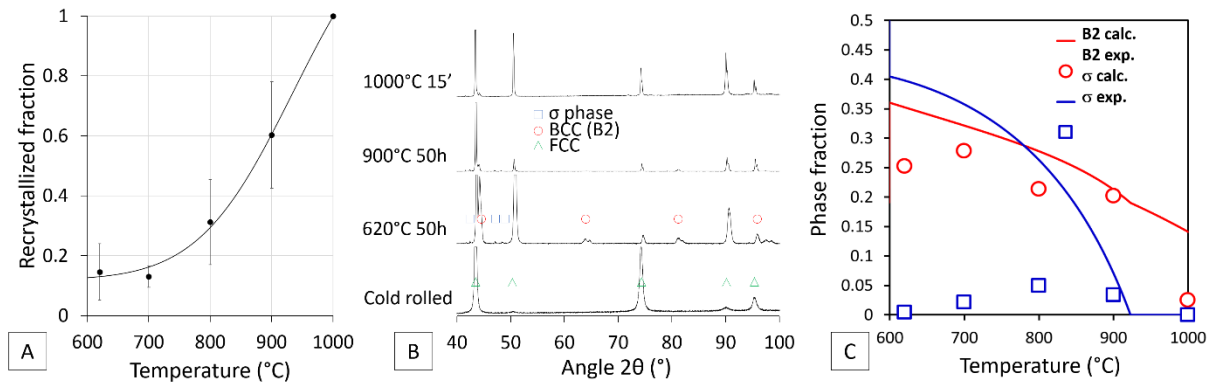


Fig. 9 Measurements performed after annealing treatments of 50 hours at various temperatures. (A) Evolution of the recrystallized FCC fraction. (B) XRD diffractograms. (C) Experimental and calculated evolutions of the volume fractions of the B2 and σ phases with the annealing temperature.

3.3. Effect of cold rolling strain

The evolution of the recrystallized volume fraction during annealing at 900°C is reported in **Fig. 10** for both thermomechanical routes. It is clear that the recrystallization kinetics is much faster after a cold rolling reduction of 80%. Indeed, 50% of the microstructure is recrystallized after 20 hours for CR58 specimens while it takes 5 minutes for CR80 specimens. Complete recrystallization is achieved in CR80 after 20 hours of annealing while it is never reached for CR58 even after 744 hours of annealing. It saturates at a recrystallization fraction of 70%.

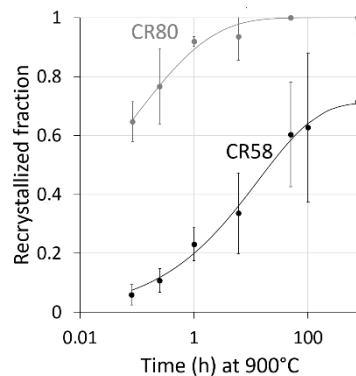


Fig. 10 Recrystallized fractions versus annealing time at 900°C after CR58 and CR80.

The microstructure of CR80-900°C/50h is composed of recrystallized and equiaxed FCC grains along with equiaxed B2 and σ grains (**Fig. 11**). The mean grain sizes are $5 \pm 0.3 \mu\text{m}$ and $1.4 \pm 0.3 \mu\text{m}$ for the FCC and the second phases, respectively. The hardness is $227 \pm 3 \text{HV}0.5$.

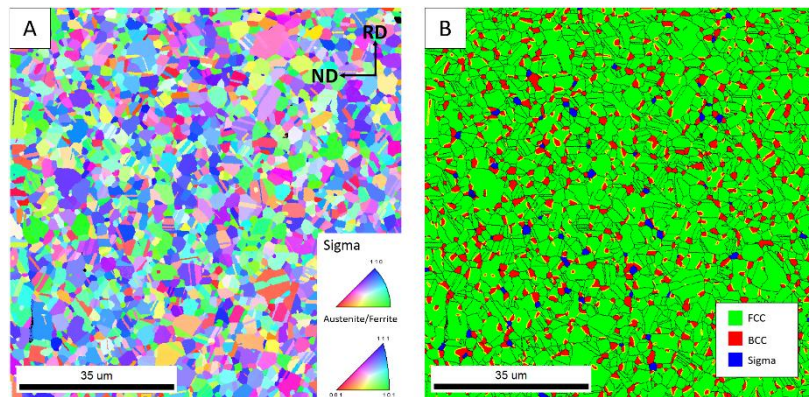


Fig. 11 EBSD maps of CR80-900°C/50h. (A) IPF map, (B) phase map.

Fig. 12a presents the microstructure of CR80-900°C/5min. **Fig. 12a** is divided in two partitions corresponding to RXZs (**Fig. 12c**) and deformed grains (**Fig. 12e**). These partitions are separated according to their grain orientation spread (GOS). This index is calculating for each grain the intensity of the deviation in orientation from its mean orientation. When this index is larger than 4° , the corresponding grain is considered as unrecrystallized. **Fig. 12b, d** and **f** present the crystallographic textures ($\varphi_2=45^\circ$ ODF sections) calculated for the whole microstructure, for the RXZs (more than 30,000 grains) and nRXZs (400 grains), respectively. All three textures are similar with maxima close to Goss and Brass. The corresponding maximum intensities are 10.8, 7.5 and 48.0. The texture of deformed grains is six times stronger than the texture of RXZs.

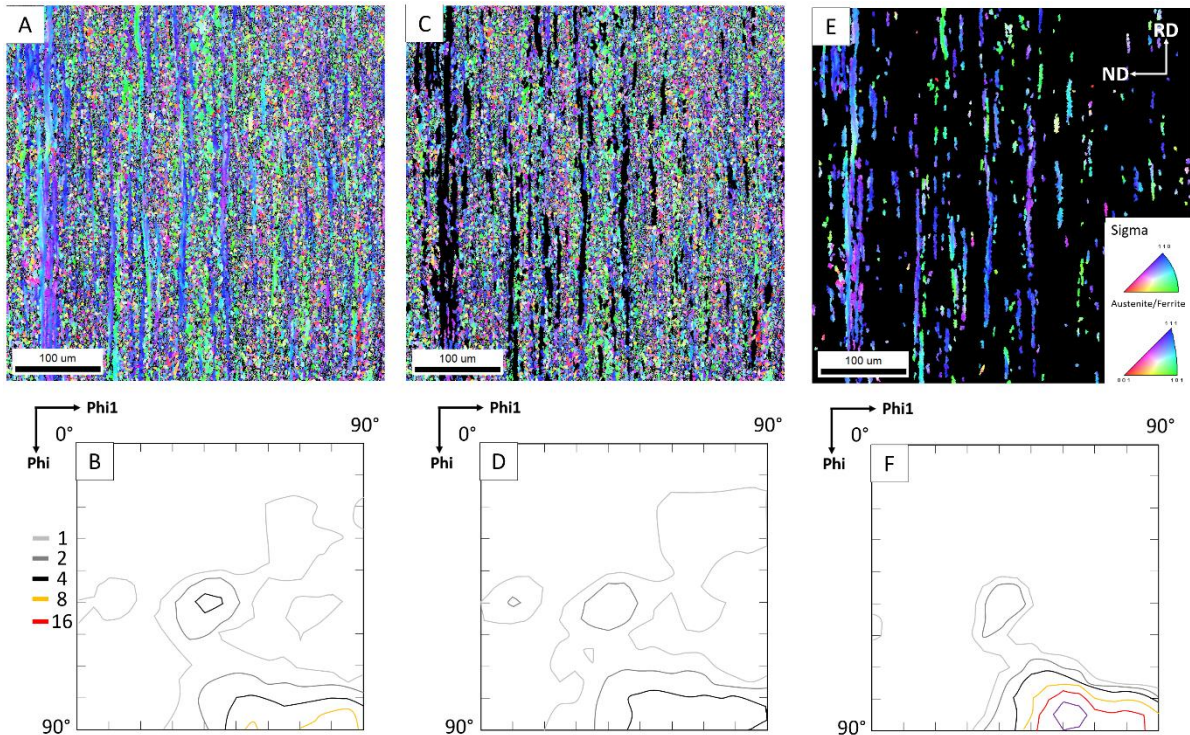


Fig. 12 CR80-900°C/5min. (A-B) correspond to the whole microstructure. (C-D) are limited to RXZs. (E-F) are limited to deformed regions (with the threshold $GOS > 4^\circ$). (A, C and F) IPF maps, (B, D and F) crystallographic textures, $\Phi_2 = 45^\circ$ ODF section.

3.4. Tensile properties

Fig. 13 presents the tensile curves for three microstructure states of C6Al. The true stress – true strain curves are given in solid lines while the work-hardening rates are shown in dotted lines. The corresponding microstructure features are given in **Table 3** along with the corresponding tensile properties.

The blue curve corresponds to a supersaturated FCC solid solution with a mean grain size is $72 \pm 2 \mu\text{m}$. It was obtained after CR80-1200°C/2min to ensure the absence of any precipitation. It presents the largest uniform elongation of 56% and the lowest yield strength of 300 MPa. Its work-hardening rate stabilizes and even increases during plastic deformation before decreasing until necking.

The red curve corresponds to a fully recrystallized microstructure containing 15% of B2 and 5% of σ grains that formed on FCC grain boundaries. The mean grain sizes are $3.7 \pm 0.3 \mu\text{m}$ and $0.9 \pm 0.2 \mu\text{m}$ for FCC and B2 grains, respectively. This microstructure was obtained after

CR80-900°C/6h. It presents a uniform elongation of 20% with a yield strength of 620 MPa. Its work-hardening rate steadily decreases until necking.

The orange curve corresponds to a heterogeneous microstructure composed of 60% of RXZs and 40% of nRXZs. It was obtained after CR80-900°C/5min. An IPF map of the corresponding microstructure is presented in **Fig. 12a**. The RXZs consist of FCC grains and intergranular B2 σ grains with mean grain sizes of $1.4 \pm 0.3 \mu\text{m}$ and $0.5 \pm 0.1 \mu\text{m}$ for FCC and the second phases, respectively. The nRXZs are composed of elongated and deformed FCC grains with length exceeding $100 \mu\text{m}$ containing fine and elongated B2 grains. These B2 grains present length of $135 \pm 70 \text{ nm}$ and width of $50 \pm 15 \text{ nm}$ measured from SEM images. The overall second phase fractions are 11% of B2 and 2% of σ . The corresponding true stress – true strain curve presents a uniform elongation of 7% with a yield strength of 1050 MPa. As for the red curve, the work-hardening rate constantly decreases during plastic deformation until failure.

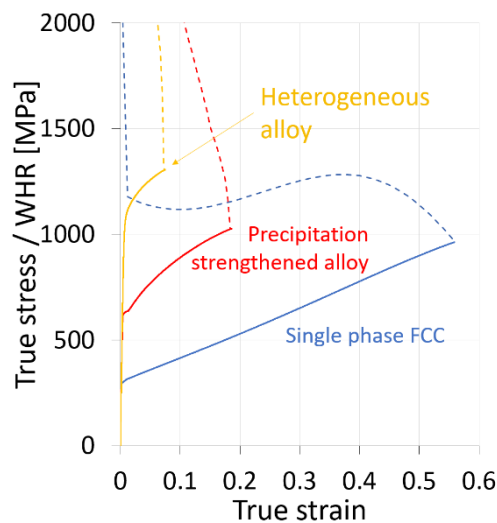
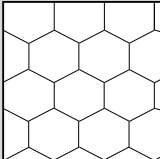
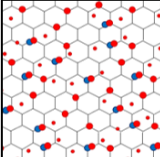
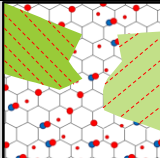


Fig. 13 Tensile curves for three microstructure states of C6Al. The true stress – true strain curves are shown in solid lines while the work-hardening rates are given with dotted lines. The blue curve corresponds to a supersaturated FCC solid solution. The red curve corresponds to a fully recrystallized microstructure containing B2 grains. The orange curve corresponds to a heterogeneous microstructure containing RXZs and nRXZs. The reader is referred to **Table 3** for further details on the corresponding microstructure features and tensile properties.

Table 3 Microstructure features of the three microstructure states of C6Al characterized in tension. The tensile properties of each states are also given.

Microstructure	RXZ fraction	Volume fractions	RXZ FCC grain size	Yield strength	Tensile strength	Uniform elongation
----------------	--------------	------------------	--------------------	----------------	------------------	--------------------

	B2		σ				
				(μm)	(MPa)	(MPa)	
Single phase microstructure (blue curve)							
	1	0	0	72 ± 2	300	630	0.56
Precipitation strengthened microstructure (red curve)							
	1	0.15	0.05	3.7 ± 0.3	620	870	0.20
Heterogeneous microstructure (orange curve)							
	0.6	0.11	0.02	1.4 ± 0.3	1050	1215	0.07

4. Discussion

4.1. Deformed state

The microstructure after cold rolling (**Fig. 4a**) consists of elongated grains presenting (i) large orientation gradients and (ii) mechanical twins. The formation of orientation gradients is typical of a material deforming by dislocation glide. Although the exact nature and structure of dislocations in HEA is still the topic of fundamental research [92], it is natural to compare the present alloy to austenitic stainless steels, especially in view of its Cr content and its FCC structure [93,94]. Unlike most austenitic stainless steels, C6Al does not undergo strain-induced martensitic transformation (**Fig. 4b**). It rather deforms by mechanical twinning. This makes the present alloy comparable to Twinning-Induced Plasticity (TWIP) steels [95]. Those comparisons are further supported by the deformation texture presented in **Fig. 4c** consisting of the α fibre with a maximum close to the Goss component. Such rolling texture are commonly reported in both austenitic stainless steels [94] and TWIP steels [95,96].

The activation of mechanical twinning is commonly attributed to a low stacking fault energy (SFE), as it is the case in TWIP steels [97]. In those steels, SFE values ranging between 20 and

50 mJ/m² are often reported [98,99]. In the case of Cantor's alloy, Zaddach *et al.* calculated using *ab initio* calculations a SFE between 18 and 27 mJ/m² [100] while the presence of twins after deformation was also confirmed experimentally [8].

The influence of Al content on the SFE of Al_xCoCrFeMnNi alloys can be calculated based on the thermodynamic modelling approach proposed by Olson and Cohen [101] and adopted by several authors [102,103]. In this model, the SFE represents the Gibbs energy required to create two layers of hexagonal close-packed (ϵ_{HCP}) phase separated from the face-centred cubic (γ_{FCC}) matrix by two interfaces:

$$\gamma_{\infty} = 2\rho\Delta G^{\gamma\rightarrow\epsilon} + 2\sigma^{\gamma/\epsilon}$$

where γ_{∞} is the ideal SFE (mJ/m²), ρ is the surface density of atoms in the {111} planes, $\sigma^{\gamma/\epsilon}$ is the surface energy of the interface γ/ϵ , and $\Delta G^{\gamma\rightarrow\epsilon}$ is the difference in Gibbs free energy of the FCC and HCP phases. The term $\Delta G^{\gamma\rightarrow\epsilon}$ can be calculated from the Gibbs energy descriptions of the involved phases using the TCHEA4 database. However, large extrapolations from the thermodynamic models in the central region of the compositional space (e.g. CoCrFeMnNi) may lead to inaccurate evaluations of the Gibbs energies [104]. To overcome this problem, the present study utilizes the SFE value determined by Zaddach *et al.* for the CoCrFeMnNi alloy as a reference to adjust the estimate from CALPHAD for the Al_{0.32}CoCrFeMnNi. The result of the calculation suggests that Al addition increases the SFE by 60% for the Al_{0.32}CoCrFeMnNi (~30-40 mJ/m²) as compared to the Cantor alloy (18-27 mJ/m²).

Liu *et al.* measured experimentally the SFE of another alloy close to CoCrFeMnNi: Al_{0.1}CoCrFeNi. He reported a value around 30 mJ/m² [65] which is slightly larger than the SFE of CoCrFeNi reported at 28 mJ/m² [100]. The authors linked the presence of deformation twins after cold rolling with this low SFE [65]. This experimental result agrees with the calculation performed above on C6Al about the increase in SFE due to the addition of aluminium.

Nevertheless, the addition of aluminium in CoCrFeMnNi, until at least 6 at.%, does not seem sufficient to suppress mechanical twinning during rolling at ambient temperature.

4.2. *Microstructure evolution during annealing*

4.2.1. A bird's eye view

Three situations can be observed according to the annealing temperature. Below 900°C, the microstructure evolution is governed by precipitation. At 900°C, precipitation and recrystallization occur simultaneously. Above 900°C, recrystallization is the main phenomenon taking place.

Below 900°C, precipitation is governing the microstructure evolution of the material. In CR58-620°C/50h, the precipitation fraction was measured at 25%, close to the value predicted by CALPHAD (**Fig. 9c**). Precipitation is coupled to a limited recrystallization. In the same sample, the recrystallization fraction is below 20% after 50 hours of annealing treatment (**Fig. 9a**). Recrystallization happens where the stored energy is the largest, i.e. along grain boundaries and shear bands (**Fig. 8a**). Co-precipitation of B2 and σ phases is also observed there (**Fig. 8b**). The overall precipitation fraction, exceeding the recrystallized fraction, infers that a large fraction of B2 grains is present inside nRXZs. However, most likely due to their small size, they were not observed with SEM.

The limited recrystallization coupled to the precipitation of fine B2 grains in nRXZs result in a hardening of 145 HV compared to the cold rolled state after 50 hours of annealing treatment at 620°C.

Above 900°C, recrystallization is the main phenomenon taking place. Compared to lower annealing temperatures where 50 hours is not sufficient to recrystallize completely the material (**Fig. 9a**), it is completed after less than 15 minutes at 1000°C (**Fig. 8c**). This increased rate can be correlated to the negligible precipitation (**Fig. 8d**). The B2 fraction was measured by both EBSD and XRD to be below 3% (**Fig. 9c**). The negligible precipitation also results in

significant grain growth inducing a decrease of the hardness level of about 170 HV after 15 minutes at 1000°C compared to the cold rolled state.

At 900°C, both recrystallization and precipitation are activated. The microstructure sequence can be summarized in three steps: (i) recrystallization, (ii) precipitation and (iii) interactions between these two phenomena. As both mechanisms activate and interact, the description of this microstructure sequence at 900°C is more complex. It is studied in detail in the next section.

4.2.2. Recrystallization and precipitation behaviour at 900°C

We will focus first on recrystallization.

Recrystallization is activated first where the stored energy is the highest, i.e. along grain boundaries [105] and shear bands [106]. Recrystallized grains form in bands following these defects as observed after 5 minutes of annealing in **Fig. 7a**.

After recrystallization occurred on these defects, it activates in the inside regions of grains. **Fig. 14** shows that GOS and Taylor factors (M) are correlated. Grains with high M present high GOS, meaning large misorientation gradients. These grains recrystallize during the annealing treatment and become RXZs. Grains with low M present low GOS meaning low misorientation gradients. These grains do not recrystallize during the annealing treatment and become nRXZs.

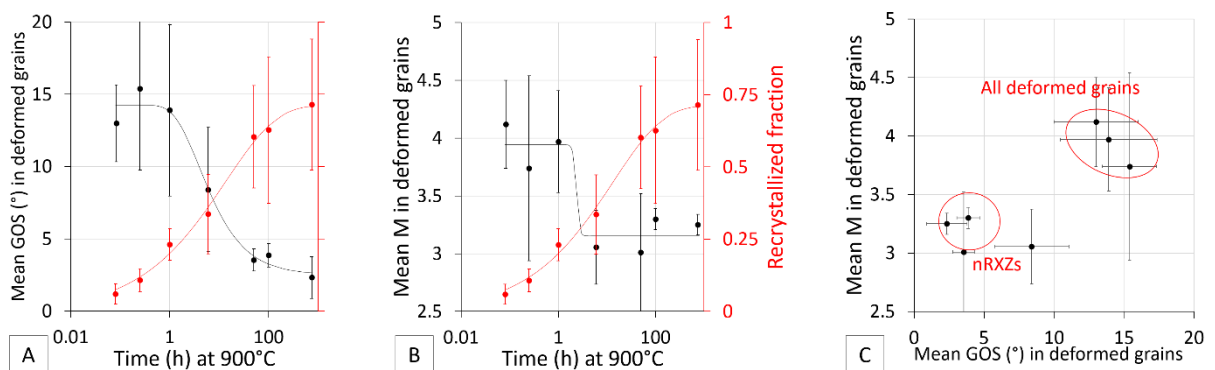


Fig. 14 (A) Mean GOS (M) and (B) mean Taylor factor (M) in deformed grains vs annealing time in CR58- 900°C. The evolution of the recrystallized fraction is given for comparison purposes. (C) Correlation between Taylor factor and GOS for the deformed grains at the beginning of annealing and for the nRXZs.

The measures of the crystallographic textures of **Fig. 12** indicate that the grains that did not yet recrystallize (**Fig. 12e**) present orientations spreading from Goss to Brass (**Fig. 12f**). According to literature, these orientations correspond to low values of M , i.e. 2.4 – 3.3 [107,108]. This is consistent with the results of **Fig. 14**. Grains presenting orientations between Goss and Brass present a delay or an absence of recrystallization.

Interestingly, although their intensities differ in a large way, the deformed (**Fig. 12f**) and recrystallized (**Fig. 12d**) textures are very similar. This is consistent with literature on multicomponent alloys presenting low SFE, such as Cantor's alloy [109] and CoCrFeNi [110], as well as in TWIP steels [111]. These similarities were attributed to the absence of preferential nucleation and growth during recrystallization.

We will now turn to precipitation. It occurs in two steps.

First, precipitates form on the new recrystallized grain boundaries. This precipitation on grain boundaries is observed after 5 minutes of annealing (**Fig. 7a**). The precipitates consist of equiaxed B2 and σ grains, the latter sharing a boundary with at least one B2 grain (**Fig. 5b**). To precise the precipitation sequence, it is interesting to look at the onset driving forces for nucleation (ODFN) of the precipitates. ODFN is the molar Gibbs energy change for the formation of the precipitate of the critical composition from the supersaturated matrix. The maximum driving force for precipitation is obtained by finding the parallel tangent surfaces passing through the alloy composition of the matrix and the precipitate Gibbs free energy curves. Positive values of ODFN indicate that precipitation is thermodynamically possible. The ODFN from the supersaturated FCC solid solution of both B2 (red line) and σ (blue line) phases were calculated using the CALPHAD method (**Fig. 15a**).

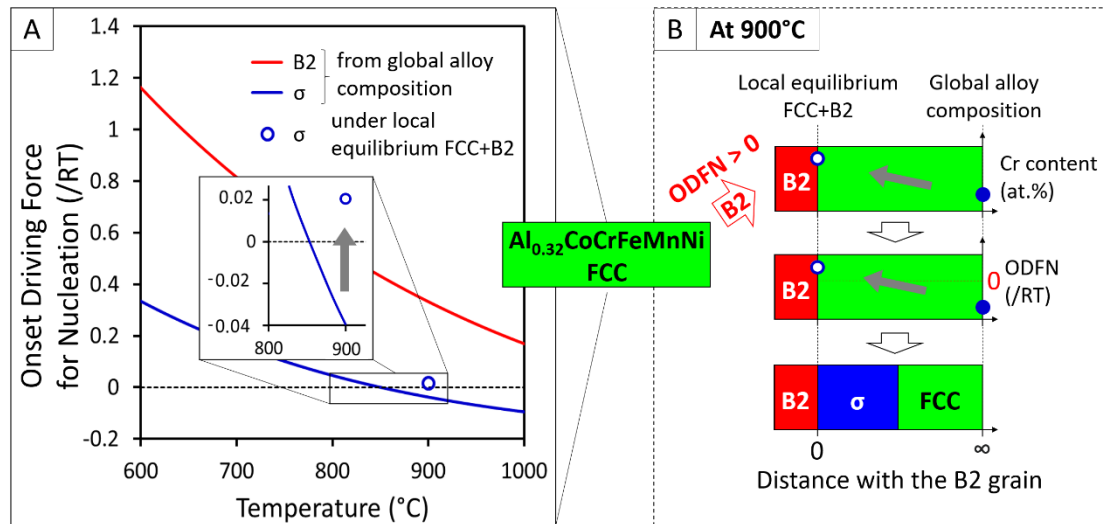


Fig. 15 (A) Onset driving forces for nucleation (ODFN) calculated with CALPHAD from the supersaturated FCC matrix of composition $Al_{0.32}CoCrFeMnNi$ for the B2 (red line) and σ (blue line) phases. The open circle corresponds to the ODFN of the σ phase under the local chemical equilibrium in the FCC matrix at the B2 interface. (B) Summary of the nucleation process of the σ phase.

These calculations show that, at 900°C, there is no driving force for the precipitation of the σ phase from the supersaturated FCC matrix (of composition $Al_{0.32}CoCrFeMnNi$) while the driving force for the B2 phase is high. This explains the large discrepancy between measured and calculated fractions of sigma phase under equilibrium conditions (Fig. 8c). Therefore, (Ni, Al)-rich B2 precipitates are very likely to appear first, leading to an enrichment in chromium of the surrounding matrix. This argument along with the B2/ σ proximity infers a coupling between the nucleation of B2 and σ phases. Such coupling was already reported in austenitic stainless steels where the σ phase appears much faster, by almost two orders of magnitude, from δ -ferrite (which is B2 as is B2) than from austenite (or γ which is FCC as is the supersaturated matrix of C6Al) [112]. Such phenomenon is attributed to the large surface energy of the γ/σ interface and to the slow diffusion of substitutional elements, such as chromium, in γ [113]. Interestingly, several studies identified the δ/γ interfaces as beneficial sites for heterogeneous nucleation of the σ phase [114,115]. In order to test the possibility of heterogeneous nucleation of σ at the FCC/B2 interface, we have calculated the ODFN of the σ phase under the local equilibrium solute content in the FCC matrix at the B2 interface (mainly an increased chromium content). As shown in the zoomed view in **Fig. 15a**, at 900°C, under the local

equilibrium chemical conditions in the FCC matrix at the B2 interface, there is a thermodynamic driving force for the σ phase precipitation (open blue circle). This result is further supported by the increased σ precipitation rate that was observed in chromium enriched regions in austenitic stainless steels [116].

The complete nucleation process of the σ phase is summarized in **Fig. 15b**. The positive ODFN of the B2 phase, amongst with other elements cited above, indicates that it forms first from the supersaturated FCC solid solution of composition $Al_{0.32}CoCrFeMnNi$. Its formation results in a modification of the chemical composition of its surroundings, mainly an enrichment in chromium (upper sketch). The ODFN of the σ phase calculated under this new local equilibrium chemical composition becomes positive. The variation of the ODFN of the σ phase is depicted by a grey arrow in the zoomed view in **Fig. 15a** and in the middle sketch of **Fig. 15b**. Its ODFN being positive, the σ phase can form locally at the FCC/B2 interface (lower sketch).

In a second step, intragranular precipitation occurs in unrecrystallized regions. It is observed after 15 minutes of annealing in **Fig. 7b**. The zoomed view in **Fig. 5b** shows that these intragranular precipitates are of the B2 phase. However, almost no σ phase is present. This discrepancy is attributed to the low diffusion in the bulk of FCC grains of solute elements [113], such as chromium in which the sigma phase is enriched. This low diffusion also limits the local chromium enrichment at FCC/B2 interfaces resulting in the local positive ODFN of the σ phase. Hence, it is proposed that the formation of the sigma phase requires two necessary but not sufficient conditions: a dense network of grain boundaries and a positive ODFN. The diffusion being limited in nRXZs, the σ phase does not form there. Furthermore, it was observed in duplex stainless steels that the σ phase is less prone to form on boundaries presenting specific orientation relationships, especially K-S [117,118]. As shown by the zoomed view in **Fig. 5b**, most of the B2 precipitates in deformed grains formed with K-S ORs on all their boundaries. Hence, the absence of the σ phase in deformed regions could also be due to the presence of

these specific boundaries. The large inconsistency between measured and calculated σ fractions below 900°C (**Fig. 9c**) is explained based on the same reasoning.

Although recrystallization and precipitation were detailed separately, they do not occur subsequently. Their simultaneous activations result in interactions that will be detailed here.

As discussed previously, intragranular precipitation occurs in unrecrystallized regions after 15 minutes of annealing (**Fig. 7b**). Yet, at this stage of the annealing treatment, only 7% of the material is recrystallized compared to 71% after 744 hours (**Fig. 10**). Hence, 64% of the material recrystallized while containing intragranular B2 precipitates. The small size of these precipitates results most probably in the pinning of grain boundaries. A significative coarsening of the precipitates is then needed to decrease the pinning pressure exerted by precipitates and allow the movement of grain boundaries. This coarsening happens via the Oswald ripening mechanism: the growth of B2 grains being linked to a decrease in the precipitate density. As previously observed during the recrystallization of aluminium alloys, this process can be accompanied by a spheroidization of precipitates [119]. These modifications in the B2 grain size, density and shape are observed when comparing RXZs and nRXZs, as in **Fig. 5b** for example. Because recrystallization rate is determined by the precipitation coarsening rate, generally considered slower than boundary migration rate, this phenomenon results in the slow recrystallization kinetics observed in C6Al (**Fig. 10**).

While recrystallization proceeds, grain growth is activated within RXZs. However, the co-precipitation of B2 and σ phases on recrystallized grain boundaries limits the growth of recrystallized grains, which is also limiting the recrystallization kinetics.

4.3. Influence of rolling strain

The recrystallization kinetics are directly linked to the strain level applied by cold rolling as highlighted in **Fig. 10**. It is observed from the same figure that recrystallization is not completed after CR58 while it is the case after CR80. Indeed, when the applied strain is larger, even the grains with lower M would have a sufficient stored energy to recrystallize, limiting the fraction of nRXZs. Nonetheless, 50 hours are required to achieve complete recrystallization after a 80% cold rolling reduction. As a matter of comparison, Cantor's alloy, remaining FCC during annealing, is completely recrystallized after less than 1 hour at 900°C following a cold rolling for 80% [120]. De la Cuevas *et al.* reported that a 22% Mn-0.6% C (in weight %) TWIP steel recrystallizes entirely in one second at 900°C after cold rolling for 60% and above [121]. These comparisons confirm the slow recrystallization kinetics of the present C6Al alloy.

Apart from the difference in kinetics, the two thermomechanical routes result in similar microstructures. It is highlighted when comparing the RXZs obtained after the two routes including the same annealing treatment at 900°C for 50 hours (**Fig. 5** and **Fig. 11**). Both present equiaxed FCC, B2 and σ grains. The grain sizes after route CR80 are smaller which is mainly caused by the larger rolling strain leading to a larger nucleation rate. These similarities confirm that the microstructure formation sequence detailed above remains valid whatever the cold rolling strain. The slower kinetics induced by the lower cold rolling strain allowed the different mechanisms and their interactions to be clearly identified in the present study.

Fig. 16 summarizes with sketches the microstructure evolution at annealing temperatures of 620, 900 and 1000°C after cold rolling reduction of 58% and at 900°C after cold rolling reduction of 80%.

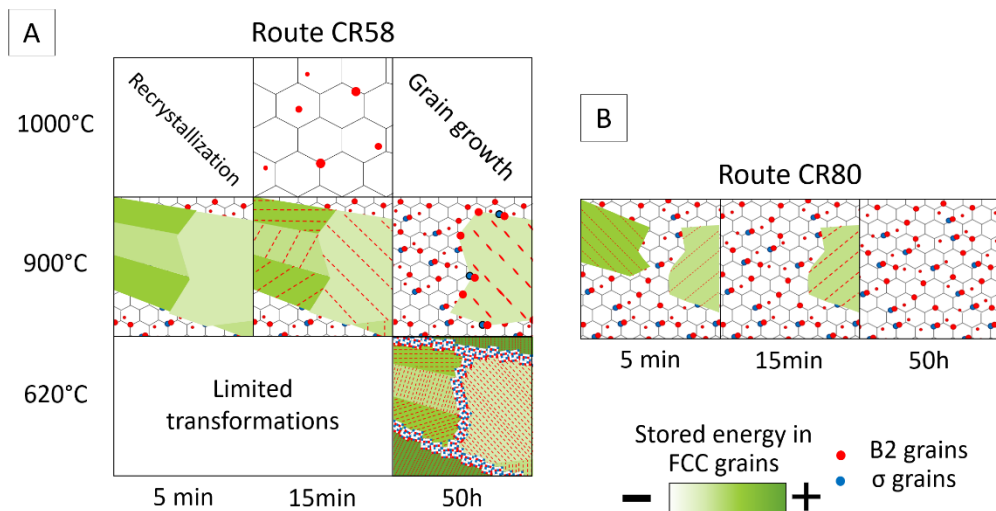


Fig. 16 Matrixes summarizing the microstructure evolutions after cold rolling reductions of (A) 58% with annealing at 620, 900 and 1000°C, and of (B) 80% with annealing at 900°C. The local stored energy in the FCC phase is depicted with shades of green. The darkest green indicates the largest stored energy while the recrystallized strain free grains are depicted in white. The second phases are shown in red for the B2 phase and blue for the σ phase.

4.4. Tensile properties

Fig. 13 shows the wide range of tensile properties that can be achieved through thermomechanical treatments from the single chemical composition C6Al. According to the microstructure states, yield strength values from 300 to 1050 MPa were recorded along with elongations from 7 to 56% (**Table 3**).

The supersaturated FCC solid solution (in blue) presents a large elongation and low yield strength that can be correlated to the hardness of the FCC phase. Moreover, this microstructure presents a remarkable work-hardening with a doubling of strength from the yield point to the tensile strength. This feature can be attributed to the activation of mechanical twinning during plastic deformation as suggested by the increasing work-hardening rate [97].

The precipitation strengthened alloy (red curve) presents a yield strength of 620 MPa, twice that of the supersaturated solid solution (in blue) of 300 MPa. This increase is mainly due to the presence of 20% of B2 and σ grains resulting in precipitation strengthening. It is also due to the decrease in grain size from 72 μm to 4 μm , resulting in grain boundary strengthening, also

known as the Hall-Petch effect. These two factors along with the absence of mechanical twinning, as suggested by the steady decrease in work-hardening rate, result in the decrease in work-hardening and uniform elongation compared to the supersaturated solid solution.

The heterogeneous alloy (orange curve) presents a yield strength of 1050 MPa, increasing of 400 MPa compared to the precipitation strengthened alloy (red curve). The corresponding microstructure is composed of 60% of RXZs and 40% of nRXZs. Its RXZs are similar to the microstructure of precipitation strengthened alloy (in red). A small increase in precipitation fractions and a small decrease in grain size must still be noted (**Table 3**). Nonetheless, the significant strengthening of the heterogeneous microstructure is attributed to the presence of nRXZs. As seen previously, these regions are constituted of large and deformed FCC grains containing a fine dispersion of B2 grains. Their work-hardened state along to the significant precipitation strengthening provided by the fine intragranular B2 grains are expected to result in an increased hardness of nRXZs compared to RXZs. This is supported by the increase of 30 HV in nRXZs compared to RXZs measured in CR58-900°C/50h. The difference in hardness between juxtaposed RXZs and nRXZS could result in back-stress strengthening, contributing to the strengthening of the heterogeneous alloy. Additional tests, such as loading-unloading-reloading cyclic tensile tests [122], should be undertaken to confirm this hypothesis and to quantify its contribution. Although the yield strength of the heterogeneous alloy is as high as 1050 MPa, it does not present any sign of brittleness with a gain of 165 MPa until tensile strength and a uniform elongation of 7%. The work-hardening of CR80-900°C/5min could also benefit from the juxtaposition of two phases with different deformation behaviours, softer RXZs and harder nRXZs, as was reported previously on titanium alloys [123] or on Q&P steels [16].

5. Summary and conclusions

A modified high-entropy Cantor alloy containing 6 at.% of Al was submitted to cold rolling and annealing. Two cold rolling reduction levels were studied. Small rolling reduction (58%) resulted in slow microstructure transformation rates allowing the different mechanisms involved to be decorrelated. The annealing temperature is shown to be the key parameter determining the governing microstructure transformations.

At annealing temperatures below 900°C, precipitation is the main phenomenon taking place. Above 900°C, recrystallization is governing the evolution of the microstructure. At 900°C, both mechanisms are occurring simultaneously. The energy stored in grains is the main parameter influencing the microstructure transformations. It determines where recrystallization occurs. In recrystallized regions, B2 and σ grains precipitate on newly formed grain boundaries. As previously reported in austenitic stainless steels, a coupling between the nucleation of these two phases was observed. The formation of the σ phase was explained by a local chromium enrichment at the B2/FCC interface. This was confirmed by thermodynamic calculation. Where recrystallization does not occur, fine intragranular B2 is observed. It was shown that these precipitates do not suppress recrystallization but delay it. After considerable annealing times, only the grains presenting the lowest stored energy, i.e. the grains with orientations close to Goss and Brass texture components, do not recrystallize. These grains correspond to a volume fraction around 30%. Moreover, it was shown that this microstructure sequence remains valid with an increase of the cold rolling strain up to 80%. Larger cold rolling strain results in accelerated recrystallization rates and enables a complete recrystallization of the material.

A wide range of tensile properties was achieved through thermomechanical treatments from the single chemical composition C6Al. According to the microstructure states, yield strength values from 300 to 1050 MPa were recorded along with uniform elongations from 7 to 56%.

These results give a new understanding of the microstructure sequence occurring after cold rolling in $\text{Al}_{0.32}\text{CoCrFeMnNi}$. It also gives an overview of the wide range of microstructures and mechanical properties that can be achieved from this single chemical composition by adapting the thermomechanical route.

Author contributions

Dorian Hachet: Conceptualization, Investigation, Visualization, Writing – Original draft preparation. **Stephane Gorsse:** Conceptualization, Software, Supervision, Validation, Visualization, Writing – Review and editing. **Stephane Godet:** Funding acquisition, Conceptualization, Supervision, Validation, Writing – Review and editing.

Acknowledgements

The authors are grateful to the WALinnov program from Wallonia region, Belgium, via the ENTROTOUGH project for financing this research. The authors also acknowledge M. Sinnaeve and P. Jacques and the Institute of Mechanics, Materials and Civil Engineering (IMMC) in UCL for the material casting. The authors also acknowledge L. Malet for the helpful discussions.

Data availability

The raw/processed data required to reproduce these findings cannot be shared at this time due to technical or time limitations.

References

- [1] B. Cantor, I.T.H. Chang, P. Knight, A.J.B. Vincent, Microstructural development in equiatomic multicomponent alloys, *Mater. Sci. Eng. A.* 375–377 (2004) 213–218. <https://doi.org/10.1016/j.msea.2003.10.257>.
- [2] J.-W. Yeh, S.-K. Chen, S.-J. Lin, J.-Y. Gan, T.-S. Chin, T.-T. Shun, C.-H. Tsau, S.-Y. Chang, Nanostructured High-Entropy Alloys with Multiple Principal Elements: Novel Alloy Design Concepts and Outcomes, *Adv. Eng. Mater.* 6 (2004) 299–303. <https://doi.org/10.1002/adem.200300567>.

- [3] S. Gorsse, J.-P. Couzinié, D.B. Miracle, From high-entropy alloys to complex concentrated alloys, *Comptes Rendus Phys.* 19 (2018) 721–736. <https://doi.org/10.1016/j.crhy.2018.09.004>.
- [4] J.-W. Yeh, Recent progress in high-entropy alloys, *Eur. J. Control.* 31 (2006) 633–648. <https://doi.org/10.3166/acsm.31.633-648>.
- [5] D. Ma, B. Grabowski, F. Körmann, J. Neugebauer, D. Raabe, Ab initio thermodynamics of the CoCrFeMnNi high entropy alloy: Importance of entropy contributions beyond the configurational one, *Acta Mater.* 100 (2015) 90–97. <https://doi.org/10.1016/j.actamat.2015.08.050>.
- [6] D.B. Miracle, High-Entropy Alloys: A Current Evaluation of Founding Ideas and Core Effects and Exploring “Nonlinear Alloys,” *JOM.* 69 (2017) 2130–2136. <https://doi.org/10.1007/s11837-017-2527-z>.
- [7] S. Gorsse, F. Tancret, Current and emerging practices of CALPHAD toward the development of high entropy alloys and complex concentrated alloys, *J. Mater. Res.* 33 (2018) 2899–2923. <https://doi.org/10.1557/jmr.2018.152>.
- [8] B. Gludovatz, A. Hohenwarter, D. Catoor, E.H. Chang, E.P. George, R.O. Ritchie, A fracture-resistant high-entropy alloy for cryogenic applications, *Science.* 345 (2014) 1153–1158. <https://doi.org/10.1126/science.1254581>.
- [9] C.K. Syn, J.W. Morris, S. Jin, Cryogenic fracture toughness of 9Ni steel enhanced through grain refinement, *Metall. Trans. A.* 7 (1976) 1827–1832. <https://doi.org/10.1007/BF02659812>.
- [10] J.I. Kim, C.K. Syn, J.W. Morris, Microstructural sources of toughness in QLT-Treated 5.5Ni cryogenic steel, *Metall. Trans. A.* 14 (1983) 93–103. <https://doi.org/10.1007/BF02643742>.
- [11] M. Koyama, T. Lee, C.S. Lee, K. Tsuzaki, Grain refinement effect on cryogenic tensile ductility in a Fe–Mn–C twinning-induced plasticity steel, *Mater. Des.* 49 (2013) 234–241. <https://doi.org/10.1016/j.matdes.2013.01.061>.
- [12] J.M. Zhang, H. Li, F. Yang, Q. Chi, L.K. Ji, Y.R. Feng, Effect of Heat Treatment Process on Mechanical Properties and Microstructure of a 9% Ni Steel for Large LNG Storage Tanks, *J. Mater. Eng. Perform.* 22 (2013) 3867–3871. <https://doi.org/10.1007/s11665-013-0701-1>.
- [13] S.S. Sohn, S. Hong, J. Lee, B.-C. Suh, S.-K. Kim, B.-J. Lee, N.J. Kim, S. Lee, Effects of Mn and Al contents on cryogenic-temperature tensile and Charpy impact properties in four austenitic high-Mn steels, *Acta Mater.* 100 (2015) 39–52. <https://doi.org/10.1016/j.actamat.2015.08.027>.
- [14] G. Laplanche, A. Kostka, O.M. Horst, G. Eggeler, E.P. George, Microstructure evolution and critical stress for twinning in the CrMnFeCoNi high-entropy alloy, *Acta Mater.* 118 (2016) 152–163. <https://doi.org/10.1016/j.actamat.2016.07.038>.
- [15] C. de Formanoir, S. Michotte, O. Rigo, L. Germain, S. Godet, Electron beam melted Ti–6Al–4V: Microstructure, texture and mechanical behavior of the as-built and heat-treated material, *Mater. Sci. Eng. A.* 652 (2016) 105–119. <https://doi.org/10.1016/j.msea.2015.11.052>.
- [16] P. Huyghe, L. Malet, M. Caruso, C. Georges, S. Godet, On the relationship between the multiphase microstructure and the mechanical properties of a 0.2C quenched and partitioned steel, *Mater. Sci. Eng. A.* 701 (2017) 254–263. <https://doi.org/10.1016/j.msea.2017.06.058>.
- [17] M. Gensamer, E.B. Pearsall, W.S. Pellini, J.R. Low, The Tensile Properties of Pearlite, Bainite, and Spheroidite, *Metallogr. Microstruct. Anal.* 1 (2012) 171–189. <https://doi.org/10.1007/s13632-012-0027-7>.
- [18] C.R. Hutchinson, J.F. Nie, S. Gorsse, Modeling the precipitation processes and strengthening mechanisms in a Mg–Al–(Zn) AZ91 alloy, *Metall. Mater. Trans. A.* 36 (2005) 2093–2105. <https://doi.org/10.1007/s11661-005-0330-x>.

- [19] S. Fu, H. Bei, Y. Chen, T.K. Liu, D. Yu, K. An, Deformation mechanisms and work-hardening behavior of transformation-induced plasticity high entropy alloys by in-situ neutron diffraction, *Mater. Res. Lett.* 6 (2018) 620–626. <https://doi.org/10.1080/21663831.2018.1523239>.
- [20] M.J. Yao, K.G. Pradeep, C.C. Tasan, D. Raabe, A novel, single phase, non-equiatomic FeMnNiCoCr high-entropy alloy with exceptional phase stability and tensile ductility, *Scr. Mater.* 72–73 (2014) 5–8. <https://doi.org/10.1016/j.scriptamat.2013.09.030>.
- [21] Z. Li, K.G. Pradeep, Y. Deng, D. Raabe, C.C. Tasan, Metastable high-entropy dual-phase alloys overcome the strength–ductility trade-off, *Nature*. 534 (2016) nature17981. <https://doi.org/10.1038/nature17981>.
- [22] J. Moon, Y. Qi, E. Tabachnikova, Y. Estrin, W.-M. Choi, S.-H. Joo, B.-J. Lee, A. Podolskiy, M. Tikhonovsky, H.S. Kim, Deformation-induced phase transformation of Co₂₀Cr₂₆Fe₂₀Mn₂₀Ni₁₄ high-entropy alloy during high-pressure torsion at 77K, *Mater. Lett.* 202 (2017) 86–88. <https://doi.org/10.1016/j.matlet.2017.05.065>.
- [23] J. Chen, Z. Yao, X. Wang, Y. Lu, X. Wang, Y. Liu, X. Fan, Effect of C content on microstructure and tensile properties of as-cast CoCrFeMnNi high entropy alloy, *Mater. Chem. Phys.* (2017). <http://www.sciencedirect.com/science/article/pii/S0254058417306272> (accessed January 19, 2018).
- [24] N.D. Stepanov, N.Yu. Yurchenko, M.A. Tikhonovsky, G.A. Salishchev, Effect of carbon content and annealing on structure and hardness of the CoCrFeNiMn-based high entropy alloys, *J. Alloys Compd.* 687 (2016) 59–71. <https://doi.org/10.1016/j.jallcom.2016.06.103>.
- [25] Z. Wang, I. Baker, W. Guo, J.D. Poplawsky, The effect of carbon on the microstructures, mechanical properties, and deformation mechanisms of thermo-mechanically treated Fe₄₀.4Ni₁₁.3Mn₃₄.8Al₇.5Cr₆ high entropy alloys, *Acta Mater.* 126 (2017) 346–360. <https://doi.org/10.1016/j.actamat.2016.12.074>.
- [26] Z. Wu, C.M. Parish, H. Bei, Nano-twin mediated plasticity in carbon-containing FeNiCoCrMn high entropy alloys, *J. Alloys Compd.* 647 (2015) 815–822. <https://doi.org/10.1016/j.jallcom.2015.05.224>.
- [27] J.B. Seol, J.W. Bae, Z. Li, J. Chan Han, J.G. Kim, D. Raabe, H.S. Kim, Boron doped ultrastrong and ductile high-entropy alloys, *Acta Mater.* 151 (2018) 366–376. <https://doi.org/10.1016/j.actamat.2018.04.004>.
- [28] Z.G. Zhu, K.H. Ma, Q. Wang, C.H. Shek, Compositional dependence of phase formation and mechanical properties in three CoCrFeNi-(Mn/Al/Cu) high entropy alloys, *Intermetallics*. 79 (2016) 1–11. <https://doi.org/10.1016/j.intermet.2016.09.003>.
- [29] H. Shahmir, M. Nili-Ahmadabadi, A. Shafiee, T.G. Langdon, Effect of a minor titanium addition on the superplastic properties of a CoCrFeNiMn high-entropy alloy processed by high-pressure torsion, *Mater. Sci. Eng. A*. 718 (2018) 468–476. <https://doi.org/10.1016/j.msea.2018.02.002>.
- [30] N. Nayan, G. Singh, S.V.S.N. Murty, A.K. Jha, B. Pant, K.M. George, U. Ramamurty, Hot deformation behaviour and microstructure control in AlCrCuNiFeCo high entropy alloy, *Intermetallics*. 55 (2014) 145–153. <https://doi.org/10.1016/j.intermet.2014.07.019>.
- [31] B. Gwalani, S. Gorsse, V. Soni, M. Carl, N. Ley, J. Smith, A.V. Ayyagari, Y. Zheng, M. Young, R.S. Mishra, R. Banerjee, Role of copper on L12 precipitation strengthened fcc based high entropy alloy, *Materialia*. 6 (2019) 100282. <https://doi.org/10.1016/j.mtla.2019.100282>.
- [32] J.Y. He, W.H. Liu, H. Wang, Y. Wu, X.J. Liu, T.G. Nieh, Z.P. Lu, Effects of Al addition on structural evolution and tensile properties of the FeCoNiCrMn high-entropy alloy system, *Acta Mater.* 62 (2014) 105–113. <https://doi.org/10.1016/j.actamat.2013.09.037>.

- [33] I. Basu, V. Ocelík, J.ThM. De Hosson, BCC-FCC interfacial effects on plasticity and strengthening mechanisms in high entropy alloys, *Acta Mater.* 157 (2018) 83–95. <https://doi.org/10.1016/j.actamat.2018.07.031>.
- [34] R.M. Pohan, B. Gwalani, J. Lee, T. Alam, J.Y. Hwang, H.J. Ryu, R. Banerjee, S.H. Hong, Microstructures and mechanical properties of mechanically alloyed and spark plasma sintered Al_{0.3}CoCrFeMnNi high entropy alloy, *Mater. Chem. Phys.* (2017). <https://doi.org/10.1016/j.matchemphys.2017.09.013>.
- [35] N. Stepanov, D. Shaysultanov, M. Klimova, V. Sanin, S. Zhrebtsov, Strengthening of a CoCrFeNiMn-Type High Entropy Alloy by Regular Arrays of Nanoprecipitates, *Mater. Sci. Forum.* 941 (2018) 772–777.
- [36] S.J. Sun, Y.Z. Tian, H.R. Lin, X.G. Dong, Y.H. Wang, Z.J. Zhang, Z.F. Zhang, Enhanced strength and ductility of bulk CoCrFeMnNi high entropy alloy having fully recrystallized ultrafine-grained structure, *Mater. Des.* 133 (2017) 122–127. <https://doi.org/10.1016/j.matdes.2017.07.054>.
- [37] L.J. Zhang, K. Guo, H. Tang, M.D. Zhang, J.T. Fan, P. Cui, Y.M. Ma, P.F. Yu, G. Li, The microstructure and mechanical properties of novel Al-Cr-Fe-Mn-Ni high-entropy alloys with trimodal distributions of coherent B2 precipitates, *Mater. Sci. Eng. A.* 757 (2019) 160–171. <https://doi.org/10.1016/j.msea.2019.04.104>.
- [38] Y.-X. Zhuang, X.-L. Zhang, X.-Y. Gu, Effect of Annealing on Microstructure and Mechanical Properties of Al_{0.5}CoCrFeMoxNi High-Entropy Alloys, *Entropy.* 20 (2018) 812. <https://doi.org/10.3390/e20110812>.
- [39] H.-P. Chou, Y.-S. Chang, S.-K. Chen, J.-W. Yeh, Microstructure, thermophysical and electrical properties in Al_xCoCrFeNi (0≤x≤2) high-entropy alloys, *Mater. Sci. Eng. B.* 163 (2009) 184–189. <https://doi.org/10.1016/j.mseb.2009.05.024>.
- [40] H. Diao, D. Ma, R. Feng, T. Liu, C. Pu, C. Zhang, W. Guo, J.D. Poplawsky, Y. Gao, P.K. Liaw, Novel NiAl-strengthened high entropy alloys with balanced tensile strength and ductility, *Mater. Sci. Eng. A.* 742 (2019) 636–647. <https://doi.org/10.1016/j.msea.2018.11.055>.
- [41] Y.-F. Kao, T.-J. Chen, S.-K. Chen, J.-W. Yeh, Microstructure and mechanical property of as-cast, -homogenized, and -deformed Al_xCoCrFeNi (0≤x≤2) high-entropy alloys, *J. Alloys Compd.* 488 (2009) 57–64. <https://doi.org/10.1016/j.jallcom.2009.08.090>.
- [42] D.-H. Lee, J.-M. Park, G. Yang, J. He, Z. Lu, J.-Y. Suh, M. Kawasaki, U. Ramamurty, J. Jang, Nano-graining a particle-strengthened high-entropy alloy, *Scr. Mater.* 163 (2019) 24–28. <https://doi.org/10.1016/j.scriptamat.2018.12.033>.
- [43] C. Li, J.C. Li, M. Zhao, Q. Jiang, Effect of aluminum contents on microstructure and properties of Al_xCoCrFeNi alloys, *J. Alloys Compd.* 504 (2010) S515–S518. <https://doi.org/10.1016/j.jallcom.2010.03.111>.
- [44] Z. Li, C.C. Tasan, K.G. Pradeep, D. Raabe, A TRIP-assisted dual-phase high-entropy alloy: Grain size and phase fraction effects on deformation behavior, *Acta Mater.* 131 (2017) 323–335. <https://doi.org/10.1016/j.actamat.2017.03.069>.
- [45] Z. Li, S. Zhao, H. Diao, P.K. Liaw, M.A. Meyers, High-velocity deformation of Al_{0.3}CoCrFeNi high-entropy alloy: Remarkable resistance to shear failure, *Sci. Rep.* 7 (2017) 42742. <https://doi.org/10.1038/srep42742>.
- [46] G. Liu, L. Liu, X. Liu, Z. Wang, Z. Han, G. Zhang, A. Kostka, Microstructure and mechanical properties of Al_{0.7}CoCrFeNi high-entropy-alloy prepared by directional solidification, *Intermetallics.* 93 (2018) 93–100. <https://doi.org/10.1016/j.intermet.2017.11.019>.
- [47] K. Liu, M. Komarasamy, B. Gwalani, S. Shukla, R.S. Mishra, Fatigue behavior of ultrafine grained triplex Al_{0.3}CoCrFeNi high entropy alloy, *Scr. Mater.* 158 (2019) 116–120. <https://doi.org/10.1016/j.scriptamat.2018.08.048>.
- [48] Y. Lu, Y. Dong, S. Guo, L. Jiang, H. Kang, T. Wang, B. Wen, Z. Wang, J. Jie, Z. Cao, H. Ruan, T. Li, A Promising New Class of High-Temperature Alloys: Eutectic High-Entropy Alloys, *Sci. Rep.* 4 (2014) 6200. <https://doi.org/10.1038/srep06200>.

- [49] Y. Lu, X. Gao, L. Jiang, Z. Chen, T. Wang, J. Jie, H. Kang, Y. Zhang, S. Guo, H. Ruan, Y. Zhao, Z. Cao, T. Li, Directly cast bulk eutectic and near-eutectic high entropy alloys with balanced strength and ductility in a wide temperature range, *Acta Mater.* 124 (2017) 143–150. <https://doi.org/10.1016/j.actamat.2016.11.016>.
- [50] Y. Ma, Q. Wang, B.B. Jiang, C.L. Li, J.M. Hao, X.N. Li, C. Dong, T.G. Nieh, Controlled formation of coherent cuboidal nanoprecipitates in body-centered cubic high-entropy alloys based on Al₂(Ni,Co,Fe,Cr)₁₄ compositions, *Acta Mater.* 147 (2018) 213–225. <https://doi.org/10.1016/j.actamat.2018.01.050>.
- [51] G. Qin, W. Xue, C. Fan, R. Chen, L. Wang, Y. Su, H. Ding, J. Guo, Effect of Co content on phase formation and mechanical properties of (AlCoCrFeNi)_{100-x}Cox high-entropy alloys, *Mater. Sci. Eng. A.* 710 (2018) 200–205. <https://doi.org/10.1016/j.msea.2017.10.088>.
- [52] J.C. Rao, H.Y. Diao, V. Ocelík, D. Vainchtein, C. Zhang, C. Kuo, Z. Tang, W. Guo, J.D. Poplawsky, Y. Zhou, P.K. Liaw, J.Th.M. De Hosson, Secondary phases in Al_xCoCrFeNi high-entropy alloys: An in-situ TEM heating study and thermodynamic appraisal, *Acta Mater.* 131 (2017) 206–220. <https://doi.org/10.1016/j.actamat.2017.03.066>.
- [53] L.J. Santodonato, P.K. Liaw, R.R. Unocic, H. Bei, J.R. Morris, Predictive multiphase evolution in Al-containing high-entropy alloys, *Nat. Commun.* 9 (2018) 1–10. <https://doi.org/10.1038/s41467-018-06757-2>.
- [54] Y. Tong, J.C. Qiao, Y. Yao, The constitutive model and threshold stress for characterizing the deformation mechanism of Al_{0.3}CoCrFeNi high entropy alloy, *Mater. Sci. Eng. A.* 730 (2018) 137–146. <https://doi.org/10.1016/j.msea.2018.05.109>.
- [55] W.-R. Wang, W.-L. Wang, J.-W. Yeh, Phases, microstructure and mechanical properties of Al_xCoCrFeNi high-entropy alloys at elevated temperatures, *J. Alloys Compd.* 589 (2014) 143–152. <https://doi.org/10.1016/j.jallcom.2013.11.084>.
- [56] X. Wang, W. Zhou, P. Liu, S. Song, K.M. Reddy, Atomic scale structural characterization of B2 phase precipitated along FCC twin boundary in a CoCrFeNiAl_{0.3} high entropy alloy, *Scr. Mater.* 162 (2019) 161–165. <https://doi.org/10.1016/j.scriptamat.2018.11.016>.
- [57] S.W. Wu, G. Wang, J. Yi, Y.D. Jia, I. Hussain, Q.J. Zhai, P.K. Liaw, Strong grain-size effect on deformation twinning of an Al_{0.1}CoCrFeNi high-entropy alloy, *Mater. Res. Lett.* 5 (2017) 276–283. <https://doi.org/10.1080/21663831.2016.1257514>.
- [58] T. Yang, S. Xia, S. Liu, C. Wang, S. Liu, Y. Zhang, J. Xue, S. Yan, Y. Wang, Effects of Al addition on microstructure and mechanical properties of Al_xCoCrFeNi High-entropy alloy, *Mater. Sci. Eng. A.* 648 (2015) 15–22. <https://doi.org/10.1016/j.msea.2015.09.034>.
- [59] H.Y. Yasuda, H. Miyamoto, K. Cho, T. Nagase, Formation of ultrafine-grained microstructure in Al_{0.3}CoCrFeNi high entropy alloys with grain boundary precipitates, *Mater. Lett.* 199 (2017) 120–123. <https://doi.org/10.1016/j.matlet.2017.04.072>.
- [60] C. Zhang, F. Zhang, H. Diao, M.C. Gao, Z. Tang, J.D. Poplawsky, P.K. Liaw, Understanding phase stability of Al-Co-Cr-Fe-Ni high entropy alloys, *Mater. Des.* 109 (2016) 425–433. <https://doi.org/10.1016/j.matdes.2016.07.073>.
- [61] T. Bhattacharjee, R. Zheng, Y. Chong, S. Sheikh, S. Guo, I.T. Clark, T. Okawa, I.S. Wani, P.P. Bhattacharjee, A. Shibata, N. Tsuji, Effect of low temperature on tensile properties of AlCoCrFeNi_{2.1} eutectic high entropy alloy, *Mater. Chem. Phys.* 210 (2018) 207–212. <https://doi.org/10.1016/j.matchemphys.2017.06.023>.
- [62] R. Chen, G. Qin, H. Zheng, L. Wang, Y. Su, Y. Chiu, H. Ding, J. Guo, H. Fu, Composition design of high entropy alloys using the valence electron concentration to balance strength and ductility, *Acta Mater.* 144 (2018) 129–137. <https://doi.org/10.1016/j.actamat.2017.10.058>.

- [63] K.H. Kong, K.C. Kim, W.T. Kim, D.H. Kim, Microstructural Features of Multicomponent FeCoCrNiSi_x Alloys, *Appl. Microsc.* 45 (2015) 32–36. <https://doi.org/10.9729/AM.2015.45.1.32>.
- [64] M. Laurent-Brocq, A. Akhatova, L. Perrière, S. Chebini, X. Sauvage, E. Leroy, Y. Champion, Insights into the phase diagram of the CrMnFeCoNi high entropy alloy, *Acta Mater.* 88 (2015) 355–365. <https://doi.org/10.1016/j.actamat.2015.01.068>.
- [65] J. Liu, C. Chen, Y. Xu, S. Wu, G. Wang, H. Wang, Y. Fang, L. Meng, Deformation twinning behaviors of the low stacking fault energy high-entropy alloy: An in-situ TEM study, *Scr. Mater.* 137 (2017) 9–12. <https://doi.org/10.1016/j.scriptamat.2017.05.001>.
- [66] N.L. Okamoto, S. Fujimoto, Y. Kambara, M. Kawamura, Z.M.T. Chen, H. Matsunoshita, K. Tanaka, H. Inui, E.P. George, Size effect, critical resolved shear stress, stacking fault energy, and solid solution strengthening in the CrMnFeCoNi high-entropy alloy, *Sci. Rep.* 6 (2016) 35863. <https://doi.org/10.1038/srep35863>.
- [67] F. Otto, A. Dlouhý, Ch. Somsen, H. Bei, G. Eggeler, E.P. George, The influences of temperature and microstructure on the tensile properties of a CoCrFeMnNi high-entropy alloy, *Acta Mater.* 61 (2013) 5743–5755. <https://doi.org/10.1016/j.actamat.2013.06.018>.
- [68] M. Seifi, D. Li, Z. Yong, P.K. Liaw, J.J. Lewandowski, Fracture Toughness and Fatigue Crack Growth Behavior of As-Cast High-Entropy Alloys, *JOM.* 67 (2015) 2288–2295. <https://doi.org/10.1007/s11837-015-1563-9>.
- [69] W.-R. Wang, W.-L. Wang, S.-C. Wang, Y.-C. Tsai, C.-H. Lai, J.-W. Yeh, Effects of Al addition on the microstructure and mechanical property of Al_xCoCrFeNi high-entropy alloys, *Intermetallics.* 26 (2012) 44–51. <https://doi.org/10.1016/j.intermet.2012.03.005>.
- [70] M. Wang, Z. Li, D. Raabe, In-situ SEM observation of phase transformation and twinning mechanisms in an interstitial high-entropy alloy, *Acta Mater.* 147 (2018) 236–246. <https://doi.org/10.1016/j.actamat.2018.01.036>.
- [71] Y. Wu, W.H. Liu, X.L. Wang, D. Ma, A.D. Stoica, T.G. Nieh, Z.B. He, Z.P. Lu, In-situ neutron diffraction study of deformation behavior of a multi-component high-entropy alloy, *Appl. Phys. Lett.* 104 (2014) 051910. <https://doi.org/10.1063/1.4863748>.
- [72] F. Zhang, C. Zhang, S.L. Chen, J. Zhu, W.S. Cao, U.R. Kattner, An understanding of high entropy alloys from phase diagram calculations, *Calphad.* 45 (2014) 1–10. <https://doi.org/10.1016/j.calphad.2013.10.006>.
- [73] F. Zhang, Y. Wu, H. Lou, Z. Zeng, V.B. Prakapenka, E. Greenberg, Y. Ren, J. Yan, J.S. Okasinski, X. Liu, Y. Liu, Q. Zeng, Z. Lu, Polymorphism in a high-entropy alloy, *Nat. Commun.* 8 (2017). <https://www.ncbi.nlm.nih.gov/pmc/articles/PMC5461481/> (accessed January 3, 2018).
- [74] T. Guo, J. Li, J. Wang, W.Y. Wang, Y. Liu, X. Luo, H. Kou, E. Beaugnon, Microstructure and properties of bulk Al_{0.5}CoCrFeNi high-entropy alloy by cold rolling and subsequent annealing, *Mater. Sci. Eng. A.* 729 (2018) 141–148. <https://doi.org/10.1016/j.msea.2018.05.054>.
- [75] N. Haghdadi, S. Primig, M. Annasamy, P. Cizek, P.D. Hodgson, D.M. Fabijanic, On the hot-worked microstructure of a face-centered cubic Al_{0.3}CoCrFeNi high entropy alloy, *Scr. Mater.* 178 (2020) 144–149. <https://doi.org/10.1016/j.scriptamat.2019.11.022>.
- [76] N. Kumar, Q. Ying, X. Nie, R.S. Mishra, Z. Tang, P.K. Liaw, R.E. Brennan, K.J. Doherty, K.C. Cho, High strain-rate compressive deformation behavior of the Al_{0.1}CrFeCoNi high entropy alloy, *Mater. Des.* 86 (2015) 598–602. <https://doi.org/10.1016/j.matdes.2015.07.161>.
- [77] J. Moon, J.W. Bae, M.J. Jang, S.M. Baek, D. Yim, B.-J. Lee, H.S. Kim, Effects of homogenization temperature on cracking during cold-rolling of Al_{0.5}CoCrFeMnNi high-entropy alloy, *Mater. Chem. Phys.* 210 (2018) 187–191. <https://doi.org/10.1016/j.matchemphys.2017.06.043>.

- [78] A. Patel, I. Wani, S.R. Reddy, S. Narayanaswamy, A. Lozinko, R. Saha, S. Guo, P.P. Bhattacharjee, Strain-path controlled microstructure, texture and hardness evolution in cryo-deformed AlCoCrFeNi_{2.1} eutectic high entropy alloy, *Intermetallics*. 97 (2018) 12–21. <https://doi.org/10.1016/j.intermet.2018.03.007>.
- [79] Q. Tang, Y. Huang, H. Cheng, X. Liao, T.G. Langdon, P. Dai, The effect of grain size on the annealing-induced phase transformation in an Al_{0.3}CoCrFeNi high entropy alloy, *Mater. Des.* 105 (2016) 381–385. <https://doi.org/10.1016/j.matdes.2016.05.079>.
- [80] I.S. Wani, T. Bhattacharjee, S. Sheikh, P.P. Bhattacharjee, S. Guo, N. Tsuji, Tailoring nanostructures and mechanical properties of AlCoCrFeNi_{2.1} eutectic high entropy alloy using thermo-mechanical processing, *Mater. Sci. Eng. A.* 675 (2016) 99–109. <https://doi.org/10.1016/j.msea.2016.08.048>.
- [81] D. Choudhuri, B. Gwalani, S. Gorsse, M. Komarasamy, S.A. Mantri, S.G. Srinivasan, R.S. Mishra, R. Banerjee, Enhancing strength and strain hardenability via deformation twinning in fcc-based high entropy alloys reinforced with intermetallic compounds, *Acta Mater.* 165 (2019) 420–430. <https://doi.org/10.1016/j.actamat.2018.12.010>.
- [82] B. Gwalani, S. Gorsse, D. Choudhuri, M. Styles, Y. Zheng, R.S. Mishra, R. Banerjee, Modifying transformation pathways in high entropy alloys or complex concentrated alloys via thermo-mechanical processing, *Acta Mater.* 153 (2018) 169–185. <https://doi.org/10.1016/j.actamat.2018.05.009>.
- [83] B. Gwalani, S. Gorsse, D. Choudhuri, Y. Zheng, R.S. Mishra, R. Banerjee, Tensile yield strength of a single bulk Al_{0.3}CoCrFeNi high entropy alloy can be tuned from 160 MPa to 1800 MPa, *Scr. Mater.* 162 (2019) 18–23. <https://doi.org/10.1016/j.scriptamat.2018.10.023>.
- [84] B. Gwalani, V. Soni, M. Lee, S. Mantri, Y. Ren, R. Banerjee, Optimizing the coupled effects of Hall-Petch and precipitation strengthening in a Al_{0.3}CoCrFeNi high entropy alloy, *Mater. Des.* 121 (2017) 254–260. <https://doi.org/10.1016/j.matdes.2017.02.072>.
- [85] S. Gangireddy, B. Gwalani, V. Soni, R. Banerjee, R.S. Mishra, Contrasting mechanical behavior in precipitation hardenable AlXCoCrFeNi high entropy alloy microstructures: Single phase FCC vs. dual phase FCC-BCC, *Mater. Sci. Eng. A.* 739 (2019) 158–166. <https://doi.org/10.1016/j.msea.2018.10.021>.
- [86] S. Gangireddy, B. Gwalani, K. Liu, R. Banerjee, R.S. Mishra, Microstructures with extraordinary dynamic work hardening and strain rate sensitivity in Al_{0.3}CoCrFeNi high entropy alloy, *Mater. Sci. Eng. A.* 734 (2018) 42–50. <https://doi.org/10.1016/j.msea.2018.07.088>.
- [87] S. Gangireddy, B. Gwalani, R.S. Mishra, Grain size dependence of strain rate sensitivity in a single phase FCC high entropy alloy Al_{0.3}CoCrFeNi, *Mater. Sci. Eng. A.* 736 (2018) 344–348. <https://doi.org/10.1016/j.msea.2018.09.009>.
- [88] S. Dasari, A. Jagetia, Y.-J. Chang, V. Soni, B. Gwalani, S. Gorsse, A.-C. Yeh, R. Banerjee, Engineering multi-scale B₂ precipitation in a heterogeneous FCC based microstructure to enhance the mechanical properties of a Al_{0.5}Co_{1.5}CrFeNi_{1.5} high entropy alloy, *J. Alloys Compd.* 830 (2020) 154707. <https://doi.org/10.1016/j.jallcom.2020.154707>.
- [89] J.M. Park, J. Moon, J.W. Bae, J. Jung, S. Lee, H.S. Kim, Effect of annealing heat treatment on microstructural evolution and tensile behavior of Al_{0.5}CoCrFeMnNi high-entropy alloy, *Mater. Sci. Eng. A.* 728 (2018) 251–258. <https://doi.org/10.1016/j.msea.2018.05.041>.
- [90] J.M. Park, J. Moon, J.W. Bae, D.H. Kim, Y.H. Jo, S. Lee, H.S. Kim, Role of BCC phase on tensile behavior of dual-phase Al_{0.5}CoCrFeMnNi high-entropy alloy at cryogenic temperature, *Mater. Sci. Eng. A.* 746 (2019) 443–447. <https://doi.org/10.1016/j.msea.2019.01.041>.
- [91] ASTM E562-11, Standard Test Method for Determining Volume Fraction by Systematic Manual Point Count, ASTM International, ASTM Int. West Conshohocken PA. (2011).

- [92] E. Ma, Unusual dislocation behavior in high-entropy alloys, *Scr. Mater.* 181 (2020) 127–133. <https://doi.org/10.1016/j.scriptamat.2020.02.021>.
- [93] S. Kheiri, H. Mirzadeh, M. Naghizadeh, Tailoring the microstructure and mechanical properties of AISI 316L austenitic stainless steel via cold rolling and reversion annealing, *Mater. Sci. Eng. A.* 759 (2019) 90–96. <https://doi.org/10.1016/j.msea.2019.05.028>.
- [94] B.R. Kumar, A.K. Singh, S. Das, D.K. Bhattacharya, Cold rolling texture in AISI 304 stainless steel, *Mater. Sci. Eng. A.* 364 (2004) 132–139. <https://doi.org/10.1016/j.msea.2003.08.012>.
- [95] K.K. Anand, B. Mahato, C. Haase, A. Kumar, S. Ghosh Chowdhury, Correlation of defect density with texture evolution during cold rolling of a Twinning-Induced Plasticity (TWIP) steel, *Mater. Sci. Eng. A.* 711 (2018) 69–77. <https://doi.org/10.1016/j.msea.2017.11.009>.
- [96] N.K. Tewary, S.K. Ghosh, S. Bera, D. Chakrabarti, S. Chatterjee, Influence of cold rolling on microstructure, texture and mechanical properties of low carbon high Mn TWIP steel, *Mater. Sci. Eng. A.* 615 (2014) 405–415. <https://doi.org/10.1016/j.msea.2014.07.088>.
- [97] B.C. De Cooman, Y. Estrin, S.K. Kim, Twinning-induced plasticity (TWIP) steels, *Acta Mater.* 142 (2018) 283–362. <https://doi.org/10.1016/j.actamat.2017.06.046>.
- [98] O. Bouaziz, S. Allain, C.P. Scott, P. Cugy, D. Barbier, High manganese austenitic twinning induced plasticity steels: A review of the microstructure properties relationships, *Curr. Opin. Solid State Mater. Sci.* 15 (2011) 141–168. <https://doi.org/10.1016/j.cossms.2011.04.002>.
- [99] Y.-K. Lee, S.-J. Lee, J. Han, Critical assessment 19: stacking fault energies of austenitic steels, *Mater. Sci. Technol.* 32 (2016) 1–8. <https://doi.org/10.1080/02670836.2015.1114252>.
- [100] A.J. Zaddach, C. Niu, C.C. Koch, D.L. Irving, Mechanical Properties and Stacking Fault Energies of NiFeCrCoMn High-Entropy Alloy, *JOM.* 65 (2013) 1780–1789. <https://doi.org/10.1007/s11837-013-0771-4>.
- [101] G.B. Olson, M. Cohen, A general mechanism of martensitic nucleation: Part I. General concepts and the FCC → HCP transformation, *Metall. Trans. A.* 7 (1976) 1897–1904. <https://doi.org/10.1007/BF02659822>.
- [102] S. Curtze, V.-T. Kuokkala, Dependence of tensile deformation behavior of TWIP steels on stacking fault energy, temperature and strain rate, *Acta Mater.* 58 (2010) 5129–5141. <https://doi.org/10.1016/j.actamat.2010.05.049>.
- [103] S. Allain, J.-P. Chateau, O. Bouaziz, S. Migot, N. Guelton, Correlations between the calculated stacking fault energy and the plasticity mechanisms in Fe–Mn–C alloys, *Mater. Sci. Eng. A.* 387–389 (2004) 158–162. <https://doi.org/10.1016/j.msea.2004.01.059>.
- [104] S. Gorse, O.N. Senkov, About the Reliability of CALPHAD Predictions in Multicomponent Systems, *Entropy.* 20 (2018) 899. <https://doi.org/10.3390/e20120899>.
- [105] M.F. Ashby, The deformation of plastically non-homogeneous materials, *Philos. Mag. J. Theor. Exp. Appl. Phys.* 21 (1970) 399–424. <https://doi.org/10.1080/14786437008238426>.
- [106] B.J. Duggan, W.B. Hutchinson, M. Hatherly, Recrystallization studies in 70:30 brass using a high voltage electron microscope, *Scr. Mater.* 12 (1978) 293–295.
- [107] W.F. Hosford, Plane-strain compression of aluminum crystals, *Acta Metall.* 14 (1966) 1085–1094. [https://doi.org/10.1016/0001-6160\(66\)90196-9](https://doi.org/10.1016/0001-6160(66)90196-9).
- [108] C. Shih-Chin, H. Duen-Huei, C. Yun-Kie, The effect of textures and grain shape on the shear band formation in rolled F.C.C. metals, *Acta Metall.* 37 (1989) 2031–2033. [https://doi.org/10.1016/0001-6160\(89\)90087-4](https://doi.org/10.1016/0001-6160(89)90087-4).
- [109] P.P. Bhattacharjee, G.D. Sathiaraj, M. Zaid, J.R. Gatti, C. Lee, C.-W. Tsai, J.-W. Yeh, Microstructure and texture evolution during annealing of equiatomic CoCrFeMnNi high-

- entropy alloy, *J. Alloys Compd.* 587 (2014) 544–552. <https://doi.org/10.1016/j.jallcom.2013.10.237>.
- [110] G.D. Sathiaraj, C.W. Tsai, J.W. Yeh, M. Jahazi, P.P. Bhattacharjee, The effect of heating rate on microstructure and texture formation during annealing of heavily cold-rolled equiatomic CoCrFeMnNi high entropy alloy, *J. Alloys Compd.* 688 (2016) 752–761. <https://doi.org/10.1016/j.jallcom.2016.07.155>.
- [111] L. Bracke, K. Verbeken, L. Kestens, J. Penning, Microstructure and texture evolution during cold rolling and annealing of a high Mn TWIP steel, *Acta Mater.* 57 (2009) 1512–1524. <https://doi.org/10.1016/j.actamat.2008.11.036>.
- [112] J. Barcik, The kinetics of σ -phase precipitation in AISI310 and AISI316 steels, *Metall. Trans. A.* 14 (1983) 635–641. <https://doi.org/10.1007/BF02643779>.
- [113] A.F. Padilha, P.R. Rios, Decomposition of Austenite in Austenitic Stainless Steels, *ISIJ Int.* 42 (2002) 325–327. <https://doi.org/10.2355/isijinternational.42.325>.
- [114] B. Weiss, R. Stickler, Phase instabilities during high temperature exposure of 316 austenitic stainless steel, *Metall. Mater. Trans. B.* 3 (1972) 851–866. <https://doi.org/10.1007/BF02647659>.
- [115] C.-C. Hsieh, W. Wu, Overview of Intermetallic Sigma (σ) Phase Precipitation in Stainless Steels, *Int. Sch. Res. Not.* (2012). <https://doi.org/10.5402/2012/732471>.
- [116] K. Shinohara, T. Seo, K. Kumada, Recrystallization and Sigma Phase Formation as Concurrent and Interacting Phenomena in 25%Cr-20%Ni Steel, *Trans. Jpn. Inst. Met.* 20 (1979) 713–723. <https://doi.org/10.2320/matertrans1960.20.713>.
- [117] Y.S. Sato, H. Kokawa, Preferential precipitation site of sigma phase in duplex stainless steel weld metal, *Scr. Mater.* 40 (1999) 659–663.
- [118] N. Haghdadi, D. Abou-Ras, P. Cizek, P.D. Hodgson, A.D. Rollett, H. Beladi, Austenite-ferrite interface crystallography dependence of sigma phase precipitation using the five-parameter characterization approach, *Mater. Lett.* 196 (2017) 264–268. <https://doi.org/10.1016/j.matlet.2017.03.090>.
- [119] S. j. Lillywhite, P. b. Prangnell, F. j. Humphreys, Interactions between precipitation and recrystallisation in an Al–Mg–Si alloy, *Mater. Sci. Technol.* 16 (2000) 1112–1120. <https://doi.org/10.1179/026708300101507037>.
- [120] N.D. Stepanov, D.G. Shaysultanov, M.S. Ozerov, S.V. Zhrebtsov, G.A. Salishchev, Second phase formation in the CoCrFeNiMn high entropy alloy after recrystallization annealing, *Mater. Lett.* 185 (2016) 1–4. <https://doi.org/10.1016/j.matlet.2016.08.088>.
- [121] F. De la Cuevas, A further study of the kinetics of recrystallization and grain growth of cold rolled TWIP steel, *Rev. Metal.* 54 (2018). <https://doi.org/10.3989/revmetalm.131>.
- [122] C. Zhang, C. Zhu, K. Vecchio, Non-equiatomic FeNiCoAl-based high entropy alloys with multiscale heterogeneous lamella structure for strength and ductility, *Mater. Sci. Eng. A.* 743 (2019) 361–371. <https://doi.org/10.1016/j.msea.2018.11.073>.
- [123] C. de Formanoir, G. Martin, F. Prima, S.Y.P. Allain, T. Dessolier, F. Sun, S. Vivès, B. Hary, Y. Bréchet, S. Godet, Micromechanical behavior and thermal stability of a dual-phase $\alpha+\alpha'$ titanium alloy produced by additive manufacturing, *Acta Mater.* 162 (2019) 149–162. <https://doi.org/10.1016/j.actamat.2018.09.050>.